Space Weather

RESEARCH ARTICLE
10.1029/2023SW003500

Special Section:
Understanding the interconnected sun-heliospheric-planetary system during solar minimum

Assessing the Effects of a Minor CIR-HSS Geomagnetic Storm on the Brazilian Low-Latitude Ionosphere: Ground and Space-Based Observations

F. S. Chingarandi[1], C. M. N. Candido[2], F. Becker-Guedes[1], O. F. Jonah[3], S. P. Moraes-Santos[1], V. Klausner[2], and O. O. Taiwo[1]

[1]National Institute for Space Research, INPE, Sao Jose dos Campos, Brazil, [2]University of Vale do Paraiba, UNIVAP, Sao Jose dos Campos, Brazil, [3]Center for Geospace Studies, SRI International, Menlo Park, CA, USA

Key Points:

- A minor Co-rotating Interaction Region/High-Speed Stream storm triggered a large positive ionospheric storm during deep solar minimum
- Multi-scale, periodic plasma irregularities were detected
- First characterization of equatorial plasma bubbles (EPBs) over Brazil using space-borne Global-scale Observations of Limb and Disk (GOLD) FUV 135.6 nm images and ground-based instruments

Supporting Information:

Supporting Information may be found in the online version of this article.

Correspondence to:

F. S. Chingarandi,
franksimba100@gmail.com

Citation:

Chingarandi, F. S., Candido, C. M. N., Becker-Guedes, F., Jonah, O. F., Moraes-Santos, S. P., Klausner, V., & Taiwo, O. O. (2023). Assessing the effects of a minor CIR-HSS geomagnetic storm on the Brazilian low-latitude ionosphere: Ground and space-based observations. *Space Weather*, *21*, e2023SW003500. https://doi.org/10.1029/2023SW003500

Received 27 MAR 2023
Accepted 2 JUN 2023
Corrected 21 OCT 2023

This article was corrected on 21 OCT 2023. See the end of the full text for details.

Abstract This paper investigates the effects of a minor G1 Co-rotating Interaction Region (CIR)/High-Speed Stream (HSS)-driven geomagnetic storm that occurred on (13–14 October 2018), during deep solar minimum. We used simultaneous observations from multiple instruments, namely; ground-based Global Navigation Satellite Systems (GNSS) receivers, a Digisonde, ground magnetometers, and space-based observations from the National Aeronautics and Space Administration Global-scale Observations of Limb and Disk (GOLD) and SWARM missions. This study presents a detailed picture of the low-latitude ionosphere response over the Brazilian sector during a minor storm. Our results showed that the minor CIR/HSS-driven storm caused a positive ionospheric storm of over ~20 TECU in magnitude. For the first time, periodic post-sunset irregularities and Equatorial Plasma Bubbles, equatorial plasma bubbles, were analyzed using GOLD FUV OI 135.6 nm emission, Total Electron Content (TEC) maps, Rate of TEC index, ROTI, and TEC gradients. Fluctuations in the interplanetary magnetic field B_z and changes in the thermospheric column density ratio ($\sum$O/N2) are discussed as the main sources of ionospheric changes during the storm. This paper highlights the importance of monitoring and understanding the impact of Sun-Earth interactions and provides insight into the behavior of the low-latitude ionosphere during minor geomagnetic storms.

Plain Language Summary Solar activity has been steadily declining over the past 4 solar cycles, in particular, the solar minima of Cycles 23 and 24 (2008–2009 and 2018–2019), were unusually weak in terms of solar activity. This period of low solar activity called deep Solar Minimum, provides a unique opportunity to study the behavior of the Earth's atmosphere and its interactions with the sun. Although the solar minimum of SC24 had much fewer sunspots than usual, which are the source of intense geomagnetic storms, fast solar wind streams or High-Speed Streams (HSSs) were still present. HSSs interact with the slower-moving wind, causing weak-to-moderate geomagnetic storms which have significant impact on the Geospace. These storms affect the Total Electron Content and plasma gradients in the ionosphere, which are important sources of errors and failures in positioning and navigation such as Global Navigation Satellite Systems and GBAS systems. This article discusses the effects of a minor geomagnetic storm during a deep solar minimum in 2018 on the Brazilian low-latitude ionosphere.

1. Introduction

Deep solar minimum has become synonymous with the two previous solar minima of cycles 23 (SC23) and 24 (SC24) which had the lowest levels of solar activity (LSA) in over 100 years (Aa et al., 2021; Derghazarian et al., 2021). This period was characterized by extremely low levels of solar flux, flare count, Coronal Mass Ejections (CME), and fewer geomagnetic storms (Gibson et al., 2011; Hady, 2013; Pesnell, 2020; Watari, 2017). Despite LSA, weak to moderate geomagnetic storms occur frequently and can affect the Geospace and Earth's ionosphere (Gibson et al., 2011). The thermosphere–ionosphere (TI) is very important for our understanding of space weather effects and forecasts. During quiet time, TI is influenced from below principally by tides, planetary waves, and gravity waves, GWs (Cai et al., 2021; Eastes et al., 2017; H. L. Liu, 2016). Gravity waves originate from tropospheric sources (Ajith et al., 2020; Hines, 1960; Jonah et al., 2016) and can propagate into the middle and upper atmosphere, causing perturbations in the ionosphere called Traveling ionospheric Disturbances (TIDs) (Vadas, 2007). TIDs are known to play an important role in the initiation of EPBs at the F layer bottomside (Aa et al., 2020; Abdu et al., 2009a; Ajith et al., 2020; Barros et al., 2018; Figueiredo et al., 2018). However, TI is also

Author Contributions:

Conceptualization: F. S. Chingarandi, C. M. N. Candido, F. Becker-Guedes, O. F. Jonah, S. P. Moraes-Santos, V. Klausner, O. O. Taiwo
Data curation: F. S. Chingarandi, C. M. N. Candido, F. Becker-Guedes, O. F. Jonah, S. P. Moraes-Santos
Formal analysis: F. S. Chingarandi, C. M. N. Candido, F. Becker-Guedes, O. F. Jonah
Investigation: F. S. Chingarandi, C. M. N. Candido, O. F. Jonah
Methodology: F. S. Chingarandi, C. M. N. Candido, F. Becker-Guedes, O. F. Jonah, V. Klausner
Resources: F. S. Chingarandi
Software: F. S. Chingarandi, O. F. Jonah, V. Klausner
Supervision: C. M. N. Candido, F. Becker-Guedes, O. F. Jonah
Validation: F. S. Chingarandi, C. M. N. Candido, F. Becker-Guedes, O. F. Jonah, V. Klausner
Visualization: F. S. Chingarandi, F. Becker-Guedes, O. F. Jonah
Writing – original draft: F. S. Chingarandi, C. M. N. Candido, F. Becker-Guedes, O. F. Jonah, S. P. Moraes-Santos, O. O. Taiwo
Writing – review & editing: F. S. Chingarandi, C. M. N. Candido, F. Becker-Guedes, O. F. Jonah, S. P. Moraes-Santos, V. Klausner, O. O. Taiwo

occasionally influenced by energy input from the magnetosphere through charged particles, electric currents, and penetration electric fields during geomagnetic storms (Eastes et al., 2017). This variability in the Thermosphere–Ionosphere (TI) system can be disruptive to radio communication and Global Navigation Satellite Systems (GNSS) (H. L. Liu, 2016). The forcing from below is highly variable which makes space weather forecasting challenging. Burns et al. (2004) studied the thermosphere temperature and composition responses to moderate geomagnetic storms and found that the effects of moderate geomagnetic storms were greater during solar minimum than during solar maximum. Thus, under weak background conditions, the thermosphere response is highly sensitive to geomagnetic disturbances (Burns et al., 2004). Seasonal variations in the background thermosphere also influence the response to geomagnetic storms (Burns et al., 2004). This is important at low latitudes where the greatest temperature and composition changes occur (H. L. Liu, 2016). Knowledge of pre-storm background conditions of the thermosphere–ionosphere is therefore essential to the accuracy of Space Weather forecasts (H. L. Liu, 2016).

Recent studies have reported large variations in the TI during SC24 solar minimum caused by weak geomagnetic disturbances (Aa et al., 2021; Burns et al., 2004; Cai et al., 2020a; Cai et al., 2021; Gan et al., 2020) These disturbances cause strong and long-lasting changes in the thermospheric column density ratio, $\sum$O/N2, over mid-latitudes (Cai et al., 2020b) caused by vertical winds generated at high latitudes through Joule heating and transported equatorward by neutral winds (Astafyeva et al., 2020; Cai et al., 2020b; J. Liu et al., 2012). Studies using GOLD have shown that minor and moderate geomagnetic disturbances can trigger large daytime increases in the thermospheric composition during deep minimum (Gan et al., 2020). As discussed by Burns et al. (1995), this low-latitude enhancement of atomic oxygen could be caused by the resulting equatorward and downward circulation. Large diurnal variations in the ionosphere Total Electron Content (TEC) are also associated with changes in the O/N2 ratio originating from high latitudes (Aa et al., 2021; Cai et al., 2021). In addition, the F region electron density is modulated by the O/N2 ratio (Danilov et al., 1994; Moro et al., 2021; Titheridge, 1974) which is an important parameter in quantifying thermospheric composition response (Burns et al., 2004; Cai, et al., 2020b; J. Liu et al., 2012). Furthermore, an increase (decrease) in plasma density during storms over quiet time is referred to as a positive (PS) and negative (negative storm (NS)) ionospheric storm (Prolss, 1995). PS over low latitude arises from enhancement in storm-time thermospheric composition caused by thermospheric expansion which causes upwelling of atomic Oxygen to higher altitudes where the rate of recombination is lower (Cai et al., 2020b; Cai et al., 2021; Danilov et al., 1994; Fuller-Rowell et al., 1996; J. Liu et al., 2012; Prolss, 1995).

During the descending phase and solar minimum, the most important driver of geomagnetic storms are Co-rotating Interaction Regions (CIRs). CIRs are formed when High-Speed Solar Wind Streams (HSSWSs or HSSs) from co-latitude Coronal Holes (CHs) interact with slow-moving solar wind streams, causing recurrent, weak to moderate geomagnetic activity (Candido et al., 2018; Tsurutani et al., 2006; Verkhoglyadova et al., 2011). Although less intense, the frequency and long duration of CIR/HSS-driven storms warrant more research as they can cause significant perturbations in the thermosphere-ionosphere system (Gibson et al., 2011). The mechanisms for these ionospheric storms over low latitudes, besides changes in neutral composition, are Prompt Penetration Electric Fields (PPEFs) and disturbance dynamo electric fields (DDEFs) (Candido et al., 2018; Fejer, 2011; Kelley et al., 2003). These disturbed electric fields are linked to sudden southward (northward) turning of interplanetary magnetic field (IMF) B_z leading to an eastward (undershielding) or a westward (overshielding) PPEF during the daytime. Large positive storms in TEC (~120%) during HSS/CIR-storms have been reported over the Brazilian sector during the deep minimum attributed to PPEF associated with reconnection processes and auroral activity (Candido et al., 2018; Verkhoglyadova et al., 2011). The condition for the PPEF is prolonged fluctuations as well as sudden changes in the polarity of B_z (Kelley et al., 2003; J. Liu et al., 2012; Tsurutani et al., 2006) which is responsible for ionospheric storms during the recovery phase (RP) of HSS/CIR-driven storms, which are usually long-lasting compared to CME-driven storms (Candido et al., 2018; J. Liu et al., 2012; Verkhoglyadova et al., 2011). Matamba and Habarulema (2018) reported weaker magnitude ionospheric storms over the African sector and found seasonal differences in ionospheric response during solstice and equinox attributed to changes in thermospheric composition driven by meridional winds (Danilov et al., 1994; Fuller-Rowell et al., 1996). The DDEF which is westward during the daytime, has opposite polarity to the undershielding PPEF. It is formed by high-latitude Joule heating through disturbance winds (J. Liu et al., 2012; Verkhoglyadova et al., 2011), and could also cause negative storms and suppression of the Equatorial Ionization Anomaly, EIA (Blanc & Richmond, 1980).

Brazilian low latitudes are uniquely influenced by complex electrodynamics processes which are driven by disturbance electric fields and winds. During the daytime, the fountain effect is responsible for the transport of the

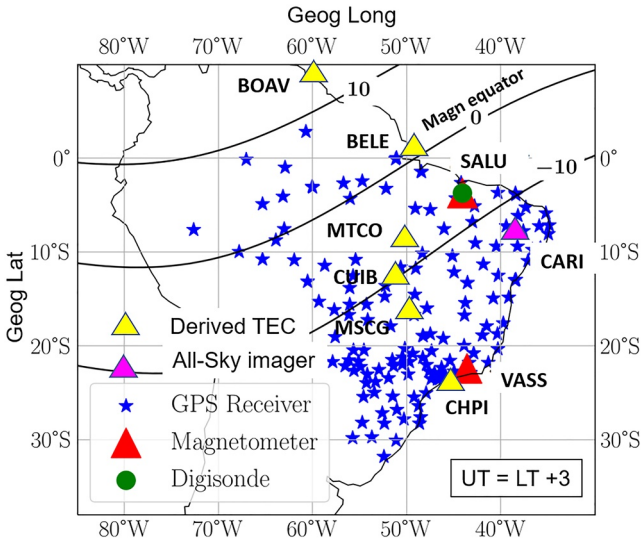

Figure 1. The blue stars represent the RBMC Global Navigation Satellite Systems receiver network with selected stations used for Total Electron Content gradients (yellow triangles). The red triangles represent the magnetometers at São Luís (SALU, dip: 3.7°S), Vassouras (VSS, dip: −20°S) and the Digisonde installed at São Luís. The magenta triangle shows the location of the all-sky imager at Cariri (dip: 12°S) shown in Figure S1 in the Supporting Information S1. The three black curves show the magnetic equator and the ±10° dip latitudes as a reference for the equatorial ionization anomaly region.

equatorial plasma to ±20° latitude, leading to the formation of two regions of higher plasma density (crests) referred to as the EIA. At sunset, there is a sudden uplift of the F layer driven by an enhanced electric field, referred to as pre-reversal enhancement (PRE) (Kelley, 2009). The PRE creates favorable conditions for the growth of Rayleigh-Taylor instability, RTI at the F layer bottomside (Abdu et al., 1981) causing the development of post-sunset plasma irregularities (EPBs) in the F-region over the equator after sunset. EPBs occur regularly from October to March in the Brazilian sector and can be strengthened or suppressed during the main and recovery phases of geomagnetic storms. These irregularities range from cm to hundreds of kilometers in size (Abdu et al., 2009b). Large gradients caused by irregularities are formed over the crests of EIA where background density is higher. The high declination angle of the magnetic field over Brazil explains the peculiar behavior of plasma irregularities over this region which occur during the equinoxes and summer solstice (Abdu et al., 1981). Alignment between the magnetic meridian and the solar terminator results in a larger PRE in the zonal electric field which controls the formation of plasma irregularities (Kelley, 2009).

In addition, the strengthening (weakening) of the daytime EIA is driven by enhancement (suppression) of the equatorial electrojet (EEJ) over low latitudes under the action of penetration electric fields and disturbance winds (Fagundes et al., 2016; J. Liu et al., 2012). The overall influence of these electric fields during intense storms depends on the local time of the storm (de Abreu et al., 2010; Fagundes et al., 2016) and can influence low-latitude electrodynamic processes that control the development of ionospheric irregularities, in some cases triggering or suppressing the RTI (Aa et al., 2021; Abdu, 2001; Abdu et al., 2009a; Moro et al., 2021). However, studies of the TI coupling system behavior during minor geomagnetic storms driven by CIR/HSS during the SC24 minimum over South America are scarce. In this work, we investigate the thermosphere and ionosphere response over the Brazilian longitudinal sector to a minor geomagnetic storm under low solar flux conditions using multiple ground and space-based observations.

2. Data and Methods

The ionospheric and thermospheric responses were investigated using thermospheric column density ratio, TEC maps, and TEC-derived parameters and indices namely: ΔTEC, Rate of TEC index, ROTI, and spatial gradients, ∇TEC; GOLD disk measurements, and SWARM in-situ electron density. The F-region parameters such as F-layer: bottom height, $h'F$, peak height h_mF_2, and critical frequency, f_0F_2 taken from Digisonde 4D measurements are also discussed. The strength of the $E \times B$ vertical drift was estimated using ground-based magnetometers over and at ∼9° off-equator (Anderson et al., 2002; Prolss, 1995). Figure 1 presents the partial South America map with the location of the Brazilian ground-based instruments used in this work. In this longitudinal sector, UT = LT + 3.

2.1. Solar and Interplanetary Parameters, and Geomagnetic Indices

The CH and HSS preliminary data were obtained from solen.info and solarmonitor.org. The solar wind and IMF parameters measured by the Advanced Composition Explorer (ACE) satellite located at Langragian point, L1 (1 **au**), as well as geomagnetic indices Kp and Sym-H were obtained from the Omniweb platform. The Auroral Electrojet, AE index was obtained from the World Data Center for Geomagnetism, Kyoto website.

2.2. GNSS TEC

TEC was calculated from the GNSS receiver's observations provided by the Brazilian Continuous Monitoring Network (RBMC), using 30-s Rinex data, managed by the Brazilian Institute for Geography and Statistics

(IBGE). The *GPS Gopi Seemala version 2.9.5* software was used to calculate the absolute TEC (more details can be found in Seemala and Valladares (2011)). Vertical TEC was obtained from the slant TEC using a mapping function at a mean ionospheric height of 350 km altitude (Misra & Enge, 2011). A cut-off elevation angle of 30° was used for all GNSS observations to minimize receiver noise and multipath errors. The receivers cover the equatorial region, dip latitude ≤5°; low latitude (EIA), 5° < dip latitude <15° and dip latitude ≥15° as low-latitude beyond the EIA respectively (Fagundes et al., 2016). Figure 1 shows the Brazilian ground-based GNSS receiver network as well as the location of ground-based magnetometers at São Luís (SALU; dip 3.7°S), obtained from the EMBRACE network while that of Vassouras (VSS dip: 20°S), an off-equatorial station was taken from the International Real-time Magnetic Observatory Network (INTERMAGNET). The Digisonde used is a DPS-4D model (UMASS Lowell) also located at São Luís.

2.2.1. Rate of TEC Index and Spatial Gradients in TEC

To investigate the occurrence and strength of plasma irregularities, the TEC-derived index, the Rate of TEC index (ROTI) was used. ROTI is defined as the standard deviation of the rate of change of TEC (ROT) over a 5 min moving window (Pi et al., 1997),

$$\mathrm{ROTI} = \sqrt{\langle \mathrm{ROT}^2 \rangle - \langle \mathrm{ROT} \rangle^2},$$

ROTI was calculated from 30 s GPS line of sight slant TEC (STEC) data and then converted to a frequency of 1 min (Pi et al., 1997). It provides information about small-scale ionospheric irregularities responsible for amplitude scintillation. The intensity of irregularities was classified as follows: ROTI ≤ 0.05 (weak irregularities); 0.05 < ROTI < 0.2 (moderate); ROTI > 0.2 (strong) (Pereira & Camargo, 2014). The vertical TEC (VTEC) is given by the following geometric relationship;

$$\mathrm{TEC} = \mathrm{STEC}\sqrt{1 - \frac{R_E^2 \mathrm{COS}^2 \in}{(R_E + h)^2}}$$

where STEC is the slant TEC, R_E is the Earth's mean radius, 6,371 km; h = 350 km is the selected altitude for the ionospheric shell.

The spatial plasma density gradients, ∇TEC, can be represented by changes in TEC with latitude or longitude (TECU/°) or with distance, (TECU/km). The time-step method was used where the differential VTEC is divided by the line-of-sight distance traveled by the IPP between two epochs for each satellite PRN (n = 1, 2, 3, 4,…N) as,

$$\nabla \mathrm{TEC}_{\|} = \frac{\mathrm{VTEC}_n(T_i) - \mathrm{VTEC}_n(T_{i-1})}{\delta s},$$

where T_i and T_{i-1} are successive epochs and δs is the distance traveled by the IPP between the two epochs. This method is very effective in the estimation of gradients at a single location and minimizes satellite biases. More details on this method are described in Lee et al. (2006) and Pradipta and Doherty (2016). TEC gradients associated with plasma bubbles come from two sources, the side walls where there are steeper gradients and weaker gradients inside the bubbles due to smaller irregularities (Pradipta & Doherty, 2016). TEC gradients are also closely related to ionospheric scintillations at EIA and may lead to severe errors and failures in GNSS and GBAS systems.

2.3. Daytime and Nighttime Disk Measurements From GOLD Instrument

The National Aeronautics and Space Administration (NASA) Global Observations of Limb and Disk (GOLD) FUV imager, on board the SES-14 communications, was launched into geostationary orbit at a central longitude of 47.5°W (Eastes et al., 2017). One of the main objectives of this mission is to study the effect of geomagnetic storms on the thermosphere and to investigate the influence of the ionosphere on the formation and evolution of EPB (Eastes et al., 2017). GOLD performs day and nighttime limb and disk scans covering the ~120°W to ~20°E longitude sector and 70°S to 70°N latitude. During the nighttime, it measures airglow emissions from 132 to 162 nm including atomic Oxygen (OI 135.6 nm) which is emission by the dominant ion at an altitude of ~300 km (Eastes et al., 2017). The airglow emission is due to radiative recombination processes whose intensity is proportional to the square of the number of electrons (Eastes et al., 2017). The OI 135.6 nm nightglow emission

is produced by the recombination of atomic Oxygen, O+ ions, and electrons and represents the spatial and temporal variations of the ionosphere. The nighttime scans have an angular spacing (E-W, N-S) and spectral resolution of 0.02 nm and 0.15° × 0.15 respectively (Eastes et al., 2017). This corresponds to 50 km × 100 km (~93 km scale size) (latitude × longitude) spatial resolution (Aa et al., 2020; Eastes et al., 2019). A single nightside sequence consists of a pair of 15-minute duration, alternate scans of the Northern and Southern hemispheres by each Channel, thereafter it simultaneously images both hemispheres from 23:10 to 00:10 UT. During the daytime, it measures the sunlit disk from 140.0 to 150.0 nm at an altitude of 160 km with a resolution of 0.2° × 0.2° and 0.04 nm spectral sampling. This spectrum includes N2 LBH bands from which the thermospheric O and N2 column density ratio ($\sum$O/N2) is derived (Eastes et al., 2017). In daytime mode, the imager scans the full disk at a 30-min cadence covering providing measurements of temperature and composition. GOLD FUV imager allowed us to have an unobstructed large-scale view with consistent daily observations as opposed to other ground instruments which are prone to weather conditions while Low Earth Orbit (LEO) satellites provide high-resolution in-situ measurements but lack spatial and temporal coverage (Aa et al., 2020). GOLD is very useful in studying the day-to-day variability of the nighttime ionosphere, particularly in remote areas such as Northern Brazil and over oceans where ground measurements are unavailable. To the best of our knowledge, this is the first time GOLD data is used to investigate the response of the ionosphere over Brazil.

2.4. SWARM In Situ Electron Density Measurements

The European Space Agency's SWARM constellation was launched in 2013 made up of three satellites in near-polar low orbits. Swarm A and C have 1.4° separation at 462 km and 87.35° inclination while Swarm B orbits at a higher altitude of 511 km. The satellites measure in-situ electron density at a much higher spatial resolution which is ideal for observing small-scale irregularities and GNSS signal loss. The data was accessed from the SWARM website.

2.5. Digisonde Data

To investigate F layer heights and frequencies behavior, we used Digisonde DPS-4 measurements installed at the equatorial station, São Luís (Geomagnetic 6.0°S, 26.7°E; Geographic 2.4°S, 44.2°W; dip latitude 3.7°S). The data was obtained from the UML Digital Ionogram Database (DIDBASE) at a cadence of 10 min. Each ionogram was manually scaled using the SAO Explorer software package, to extract the F-layer parameters; virtual height, $h'F$, peak height, h_mF_2, and critical frequency f_0F_2. These parameters are important in ascertaining the background electrodynamics conditions of the ionosphere that control the development occurrence of plasma irregularities. To quantify the storm effects, the monthly five most quiet days (5QD) average was calculated.

2.6. Estimation of Equatorial Electrojet Strength From Ground-Based Magnetometers

Near the magnetic equator, there is a large enhancement in the horizontal (H) component of the magnetic field due to an increased Cowling conductivity which leads to an intense eastward current system at around 100 km in altitude in the E region called the EEJ (Kelley, 2009). This current is a measure of the equatorial electric field and can be detected as an enhancement in the H component of the magnetometer (Anderson et al., 2002). By computing the difference between the magnitude of the H component at an equatorial site and another off the magnetic equator, the magnitude of the vertical $E \times B$ drift can be estimated (Anderson et al., 2002). The ΔH is therefore an effective method to infer the presence of penetration electric fields that may enhance or suppress the $E \times B$ drift which is a critical factor in the development of the EIA and irregularities (Kelley, 2009). The horizontal component ΔH was computed by using two magnetometers located at SALU and Vassouras as shown in Figure 1.

3. Results

3.1. CIR/HSS-Driven Geomagnetic Storm on 13–14 October 2018

On 13 October 2018, a minor geomagnetic storm (minimum *Sym-H* − 50 nT) was driven by a CIR/HSS. Figure 2 presents the solar disk image captured by the Dynamics Observatory (Solar Dynamics Observatory) at wavelength 195 Å on 10 October 2018 showing a trans-equatorial CH (CH889) on the solar disk ~3 days before the storm.

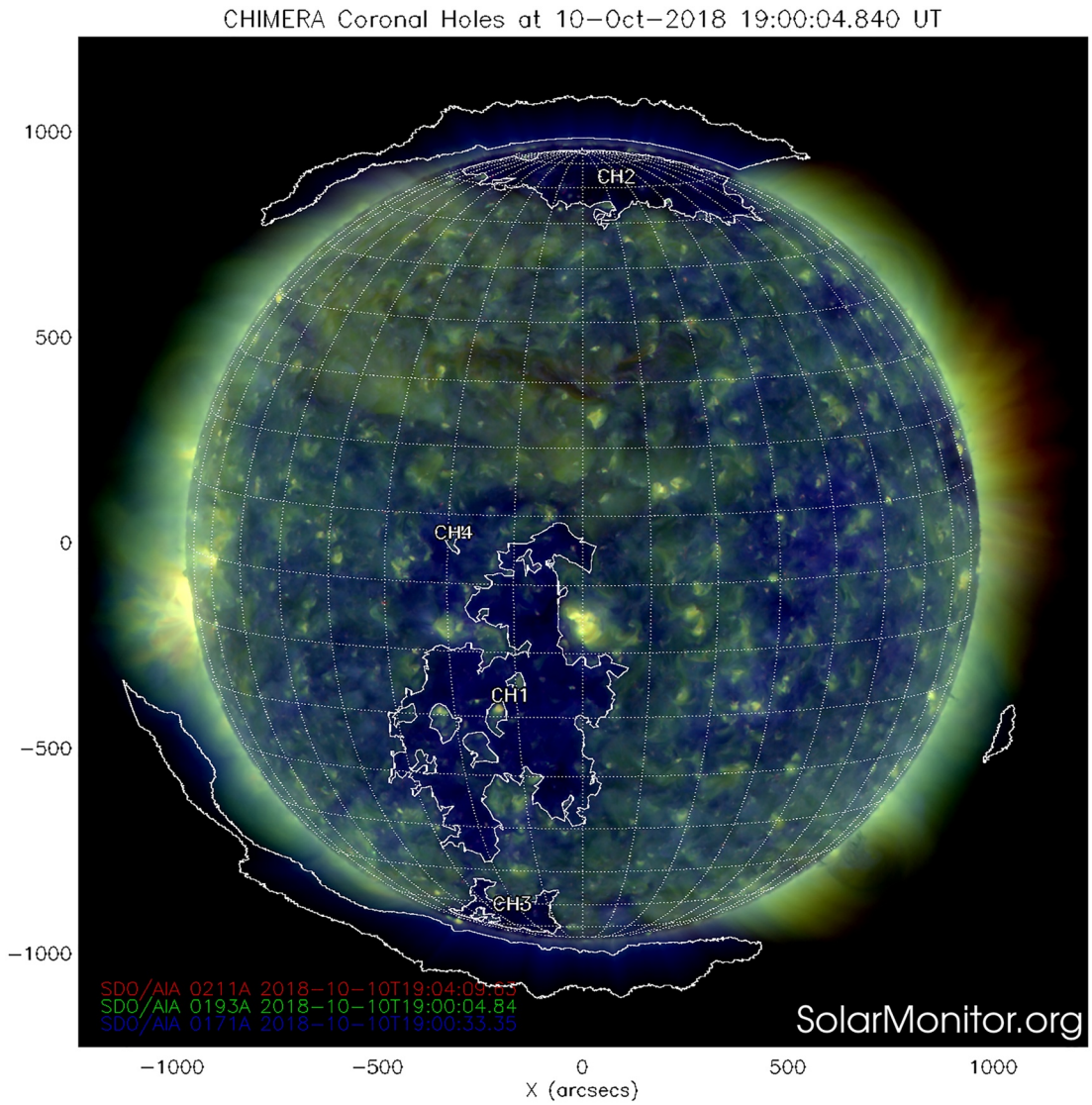

Figure 2. Trans-equatorial Coronal Hole captured by the Solar Dynamics Observatory at 193 Å wavelength on 10 October 2018. The bright emission represents an active region.

Figure 3 shows the variation of solar, interplanetary, and geomagnetic parameters from 13 to 14 October. From top to bottom panel, it is shown: the solar wind speed, Vsw (km/s), the plasma temperature, T_p (K), the proton density, N_p (n/cm^{-3}), the IMF magnitude, |B|, and its components B_x, B_y, and B_z in (nT), GSM coordinate system; the east-west component of the Interplanetary Electric Field, IEF, Ey (mV/m), the longitudinally symmetric index, Sym-H (nT), the auroral electrojet index AE (nT), the K_p index, and the solar flux index, F10.7 (in SFU) where (1 SFU = 10^{-22}W m^{-2} Hz^{-1}).

A small sudden increase in the solar wind velocity is observed at 15:00 UT (noon LT accompanied by an increase in Np and Tp, which is typical of a CIR/HSS; Tsurutani et al., 2006). The B_z abruptly turned from northward to southward within a few minutes and remained southward for more than 3 hr. There was no clear Sudden Storm Commencement, SSC, and the Sym-H minimum of −50 nT occurred at ∼19:00 UT (16:00 LT). The K_p reached a maximum of 4 during the main phase (MP) while AE increased from <100 nT to reach a peak of ∼1,300 nT during the MP. This variation in geomagnetic indices is typical of low geomagnetic activity (Aa et al., 2021; J. Liu et al., 2012). Increased auroral activity with southward B_z indicates the injection of energy through substorms and particle precipitation (Aa et al., 2021; Tsurutani et al., 1995). The MP of the storm occurred from 14:00 UT to 19:00 UT (11:00 LT to 16:00 LT) and was followed by a short RP which lasted up to 14 October, at 18:00 UT

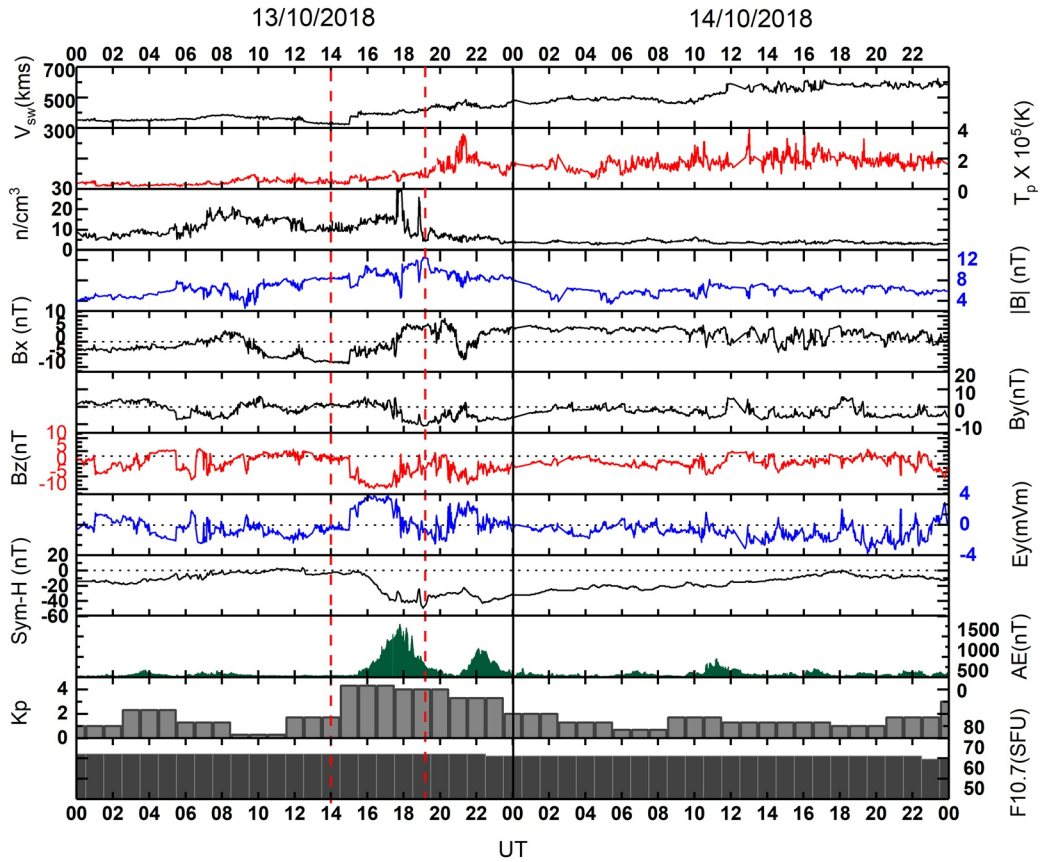

Figure 3. Variation of solar, interplanetary, and geomagnetic parameters and indices on 13–14 October 2018. From top to bottom: the solar wind speed, V_{sw} (km/s);, the plasma temperature; T_p (K), the proton density, N_p (n/cm^{-3}), the Interplanetary Magnetic Field, |*B*| (nT);, and its components B_x, B_y, B_z, the east-west component of the IEF, Ey (mV/m), the longitudinally symmetric index, Sym-H (nT), the AE index (nT), the K_p index, and the F10.7 (sfu) solar flux. The red lines indicate the beginning of the main and recovery phases.

(15:00 LT), a period of ∼23 hr. At the end of the MP, around 19:00 UT (16:00 LT), the IMF components B_x and B_y reached ∼6 nT and −10 nT, respectively. The B_z became southward and highly oscillatory from 15:00 to 21:00 UT (12:00 to 18:00 LT). After this, a new southward turning in B_z can be observed. During this geomagnetic storm, the solar flux F10.7 remained at around 70 sfu, indicating very low solar activity (Aa et al., 2021; Derghazarian et al., 2021). The v_{sw} peaked at ∼600 km/s during the RP in the second half of day 14. Following the NOAA geomagnetic storms classification, this event can be described as a minor storm, G1. It is important to note that the negative Sym-H before the storm at the beginning of 13 October is related to the end of the RP of a previous moderate storm (not studied here) also caused by a CIR/HSS.

3.2. Ionospheric Storms in TEC and Changes in Thermospheric Composition

To investigate the response of the thermosphere-ionosphere (TI) to the HSS/CIR-driven storm we analyzed the TEC over the Brazilian sector. Figure 4 shows on Top: Top hourly TEC maps obtained from ground-based GNSS receiver's observations on 13 October, from 14:00 to 23:40 UT (11:00 to 20:40 LT). The beginning of the MP and the recovery phases is indicated on the maps. (b) The bottom shows the variation of TEC, ΔTEC, which is the difference in magnitude of the TEC between the disturbed day, 13 October ($K_p > 4$), and the reference quiet day, 6 October ($K_p \leq 3$). The criteria for the quiet day were determined based on the auroral activity (AE < 250 nT) and the daily maximum planetary index ($K_p < 3$) (Cai et al., 2020b, 2021; Klenzing et al., 2013). The TEC and the ΔTEC maps were generated every 15 min; however, for the post-sunset, we only show the observations that coincide with the GOLD radiance maps (22:00–23:23:40 UT). Figure 4a (top) shows high temporal and spatial variability in TEC during the MP of the storm (MP) with strong development in the southern crest of EIA (data over the northern region is scarce).

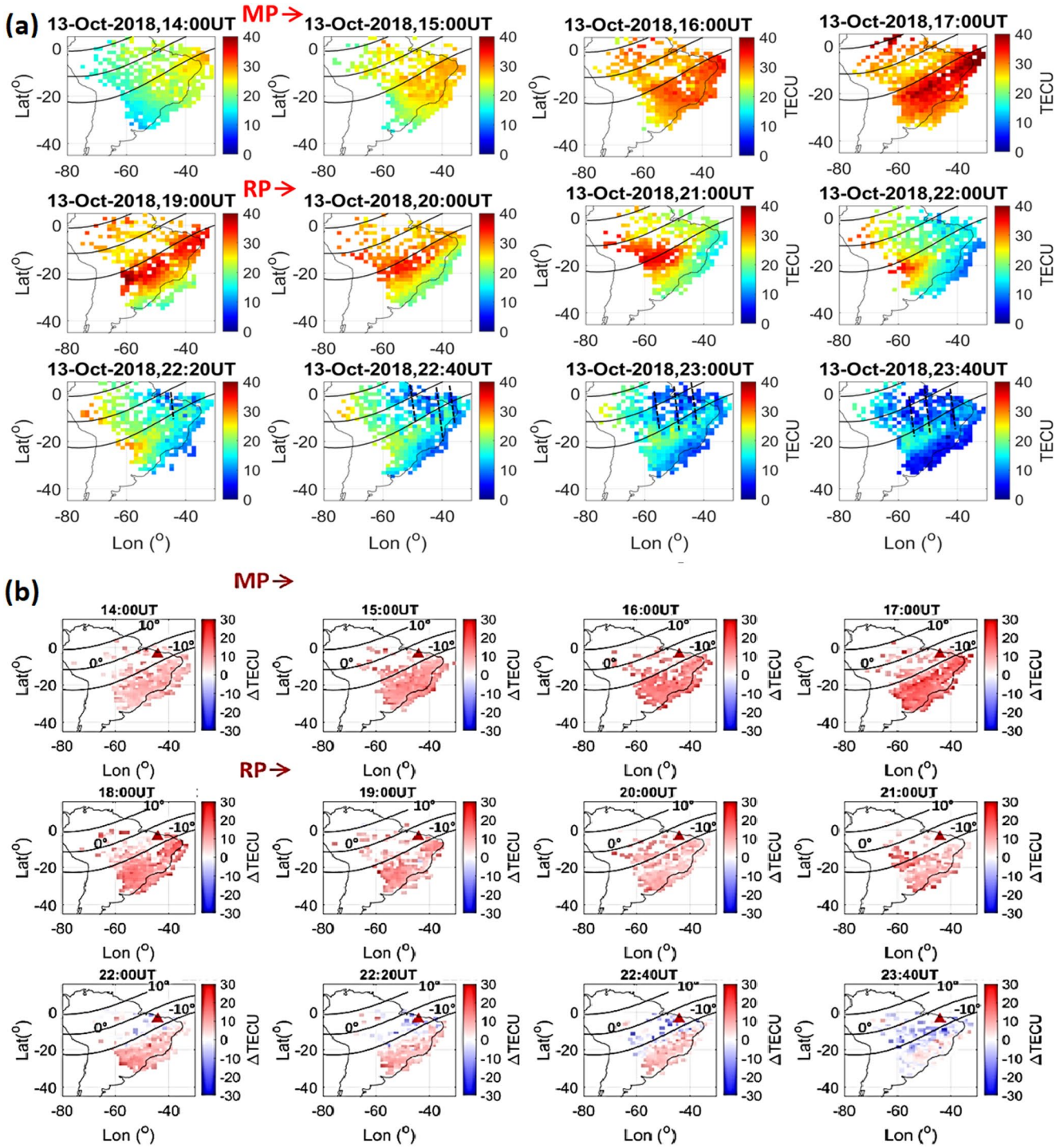

Figure 4. (a) Total Electron Content (TEC) maps and (b) ΔTEC maps over Brazil on 13 October 2018, where UT = LT + 3. The black lines represent the magnetic equator in the middle, and the outer lines represent ±10° dip latitude. The evolution of the equatorial ionization anomaly is shown in the TEC while the dotted black lines indicate equatorial plasma bubbles. ΔTEC maps show a large positive ionospheric storm followed by a negative ionospheric storm.

The EIA over the western sector of Brazil (longitude >50°W) was stronger than the eastern sector around 21:00 UT (18:00 LT). The TEC maximum, ~40 TECU, occurred at ~17:00 UT (14:00 LT) around the southern crest of the EIA (dip lat ~15°S). From ~16:00–19:00 UT (13:00–16:00 LT), the EIA expanded poleward up to dip latitude ~20°S, an expansion of ~5° latitude compared to the quiet time EIA on 06 October when it reached ~15°S dip latitude. The enhancement of the EIA during the disturbed interval indicates the strengthening of

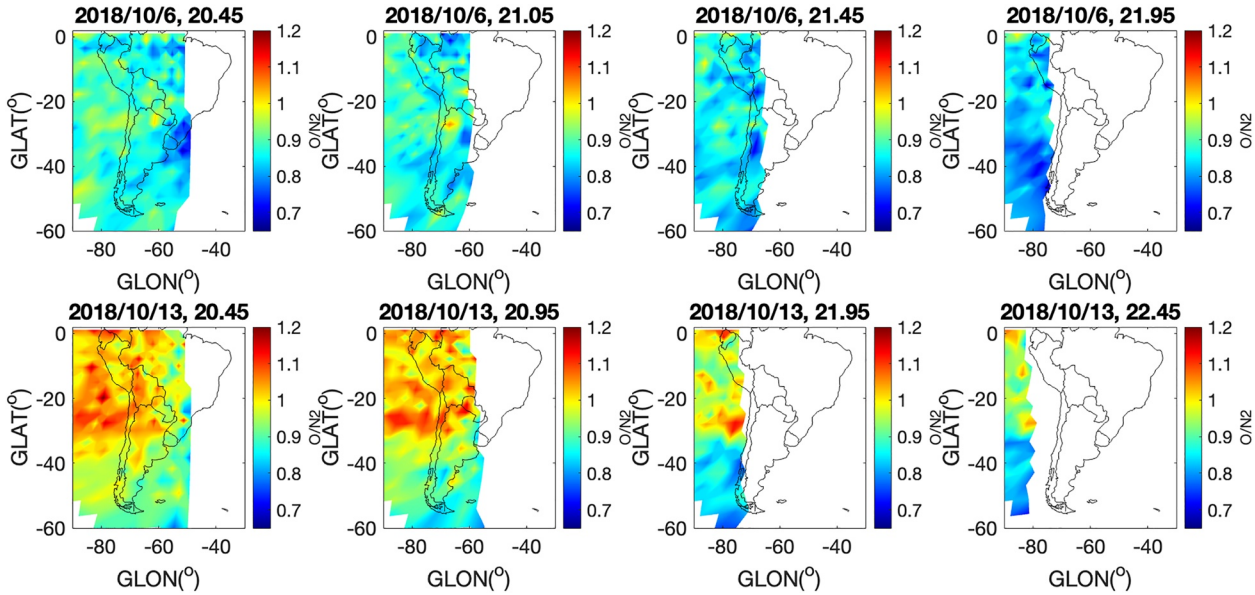

Figure 5. GOLD ∑O/N2 variation over South America from 20:45 to 22:45 UT (17:45 to 19:45 LT) on the quiet day 6 October 2018 (top row) and the disturbed day 13 October 2018 (bottom row).

$E \times B$ vertical drift under the influence of an enhanced zonal electric field, PPEF (Kelley et al., 2003; J. Y. Liu et al., 1999). At sunset, ~22:20 UT (19:20 LT in this longitude) depletions in TEC, aligned from north-southeast (dark blue structures) can be observed at ~45°W. Such depletions in TEC maps are signatures of EPBs (Aa et al., 2019; Cai et al., 2020a; Chou et al., 2020; Takahashi et al., 2015, 2016) and can be seen up to 23:40 UT (20:40 LT). Figure 4b shows intensification in TEC, ΔTEC > 0, in comparison to the quiet day, that is, a positive ionospheric storm that began just after the MP and reached a maximum of ~23 TECU around 17:00 UT (14:00 LT) over the crests of EIA. The daytime PS remained until nighttime hours, however, after sunset, it transitioned into a NS after 22:00 UT, 19:00 LT during the occurrence of EBPs, that is, closer to the geomagnetic equator (see Figures 4a and 4b). To assess the possible mechanisms responsible for the daytime ionospheric PS we consider the influence of the neutral thermospheric composition changes and prompt penetration of the electric fields during the MP of the storm. At first, we analyze the ∑O/N2 variation which plays an important role in modulating the daytime TEC during geomagnetic storms (Cai et al., 2021; Titheridge, 1974) (Rishbeth, 1998).

Figure 5 shows the variation of the column density ratio (∑O/N2) from GOLD over the South American sector from 20:45 to 22:45 UT (17:45 to 19:45 LT) and on the quiet reference day of 06 October (top row) and on 13 October (bottom row). The ∑O/N2 is available only up to an hour after sunset which is around 22:00 UT (19:00 LT). At 20:45 UT (17:45 LT), there was a 20%–30% patch-like enhancement in O/N2 over equatorial and low latitudes (0°–40° geographic latitude) compared to the quiet reference. Although there was a lack of data coverage over the eastern part of the continent, it is possible to infer that the ∑O/N2 column density ratio was higher in magnitude but decreased gradually. As seen in Figure 4b, a positive ionospheric storm of ~23 TECU began during the MP and continued during the first part of the night until ~22:40 UT (20:40 LT) whose amplitude decreased after 19:00 UT (16:00 LT). The EIA was also more pronounced (Figure 4a) (Cai et al., 2021). This increase coincided with enhancement in ∑O/N2 observed in Figure 5. The magnitude in the PS is in agreement with J. Liu et al. (2012) who found PS of 15 TECU over low latitudes during a CIR/HSS-driven storm with similar magnitude (minimum Sym-H ~ –50 nT and B_z ~ −18 nT).

The quiet day closest to the storm (day 6) was selected as the reference instead of the five quietest days (18, 19, 20, 23, and 29) since the 5QD are much further from the storm and thus could include seasonal changes which would have compounded the analysis of the thermospheric composition. Thus, the storm occurred during the period of transition into the local equinox (Bhattacharyya et al., 1992) in which there are seasonal changes in the thermospheric composition (Titheridge, 1974). The quiet background conditions in the thermosphere before a geomagnetic storm are determined by solar EUV and thus seasonal variations are very important in understanding the TI response (H. L. Liu, 2016). Thermospheric composition increases during the storm time are associated

with thermospheric expansion due to Joule heating (Cai et al., 2020b; Cai et al., 2021; Danilov et al., 1994; Fuller-Rowell et al., 1996; Prolss, 1995). This causes upwelling of the thermosphere, decreasing the neutral composition ratio and causing a PS over low latitudes (Astafyeva et al., 2015). This may explain the sustained positive storm effect in VTEC.

3.3. Equatorial Plasma Bubbles

Besides the remarkable intensification in TEC, large-scale plasma irregularities were observed as TEC depletions after 22:00 UT (19:00 LT), as shown in Figure 4a during the minor storm. The effects of intense storms caused by coronal mass ejections (CMEs) on the ionosphere which disrupt GNSS and communications (Astafyeva et al., 2015, 2020) have been studied extensively. A recent report by National Oceanic and Atmospheric Administration, NOAA, reported a minor storm in 2022 that caused the loss of 38 Starlink small satellites. More such studies are of great interest to stakeholders in the space industry as a whole. This also prompts the following question: Can a minor storm during a solar minimum significantly impact the ionosphere and space assets? Our results show an enhancement of the EIA during the daytime and a prolonged presence in the nighttime. To this, we arrive at another the question, Does this positive ionospheric storm together with a prolonged EIA enhancement at nighttime play a role in the development of plasma irregularities and consequently ionospheric scintillation in that region? To answer this, we used space and ground-based ionospheric data and parameters. For the first time airglow data provided by GOLD OI 135.6 nm radiance maps are used to characterize in detail EPBs observed over Brazil during low solar activity.

Figure 6 (top) shows a sequence of GOLD OI 135.6 nm emissions, at ∼300 km of altitude, from 21:55 UT (18:55 LT) to 23:55 UT (20:55 LT). The 135.6 nm radiance represents the F-layer peak electron density, NmF2, in the nighttime ionosphere although most of the contribution is localized at the F-layer peak height (Cai et al., 2020a). Figure 6 (bottom) shows the electron density (Ne) variation with latitude from a single pass of the satellite SWARM between 00:38 and 00:54 UT (21:38 and 21:54 LT) in the longitude ∼39°W (bottom left panel), around 50 min after the last image provided by GOLD at 23:55 UT.

The images show the post-sunset EIA which extends to ∼±15° off the equator and is seen as regions of bright radiance around the North and South of the geomagnetic equator. We also observed structured depletions, elongated in the northwest-southeast direction, associated with equatorial plasma bubbles (EPBs) whose "feet" extend to the crests of the EIA. These depletions coincide with those seen on the TEC maps shown in Figure 4a albeit at higher resolution. The westward inclination of the depletions is likely due to gradients in the zonal drift velocity which decreases with increasing latitude (Aa et al., 2020; Barros et al., 2018). The depletion in electron density was $\sim 4 \times 10^5/cm^3$ near the geographic. Sharp variations in Ne are found within ∼±15° geographic latitudes over the same region of TEC depletions (seen in the GOLD image 50 min earlier) over 39°W longitude (∼10°–15° dip latitude). These are the signatures of small-scale irregularities associated with EPBs (Aa et al., 2020). To obtain a more detailed analysis of the EPB characteristics from using two distinct techniques, we compare simultaneous observations of GOLD OI 135-nm airglow and a TEC map at 23:55 UT (20:55 LT) on 13 October 2018, as shown in Figures 7a and 7b, respectively. The scales have been adjusted to show more clearly the depletions and the EIA. The observed EIA morphology and the depletions by GOLD images and TEC maps show good agreement.

Cai et al. (2020a) showed that observations of GOLD OI 135.6 radiance and GPS TEC show good agreement in the magnitude and morphology of the EIA and depletions. However, there are some differences between the two observations. First, GOLD images have higher resolution in comparison with TEC maps. One reason is the sparse distribution of GNSS receivers in the northern region of Brazil. Second, TEC represents the integral of the electron density map to a mean shell height of 350 km (Misra & Enge, 2011) while the OI 135.6 nm represents the F layer peak electron density in the nighttime ionosphere (Cai et al., 2020a). A significant portion of the airglow emission is absorbed in the thermosphere before it reaches ground-based imagers, as such GOLD measurements are more sensitive to the weak airglow emissions in the nightside allowing the detection of fainter structures (Cai et al., 2020a).

The EPB depletions have a periodic longitudinal separation, as previously reported by Eastes et al. (2019). This can be observed in the GOLD OI 135.6 radiance maps in the 35°W–60°W sectors. In general, the estimated distance between the EPBs ranges from 300 to 500 km, and varies with latitude, while the plasma bubble width is ∼200 km. Furthermore, the depletion level between the bubble walls and surrounding plasma is around 10

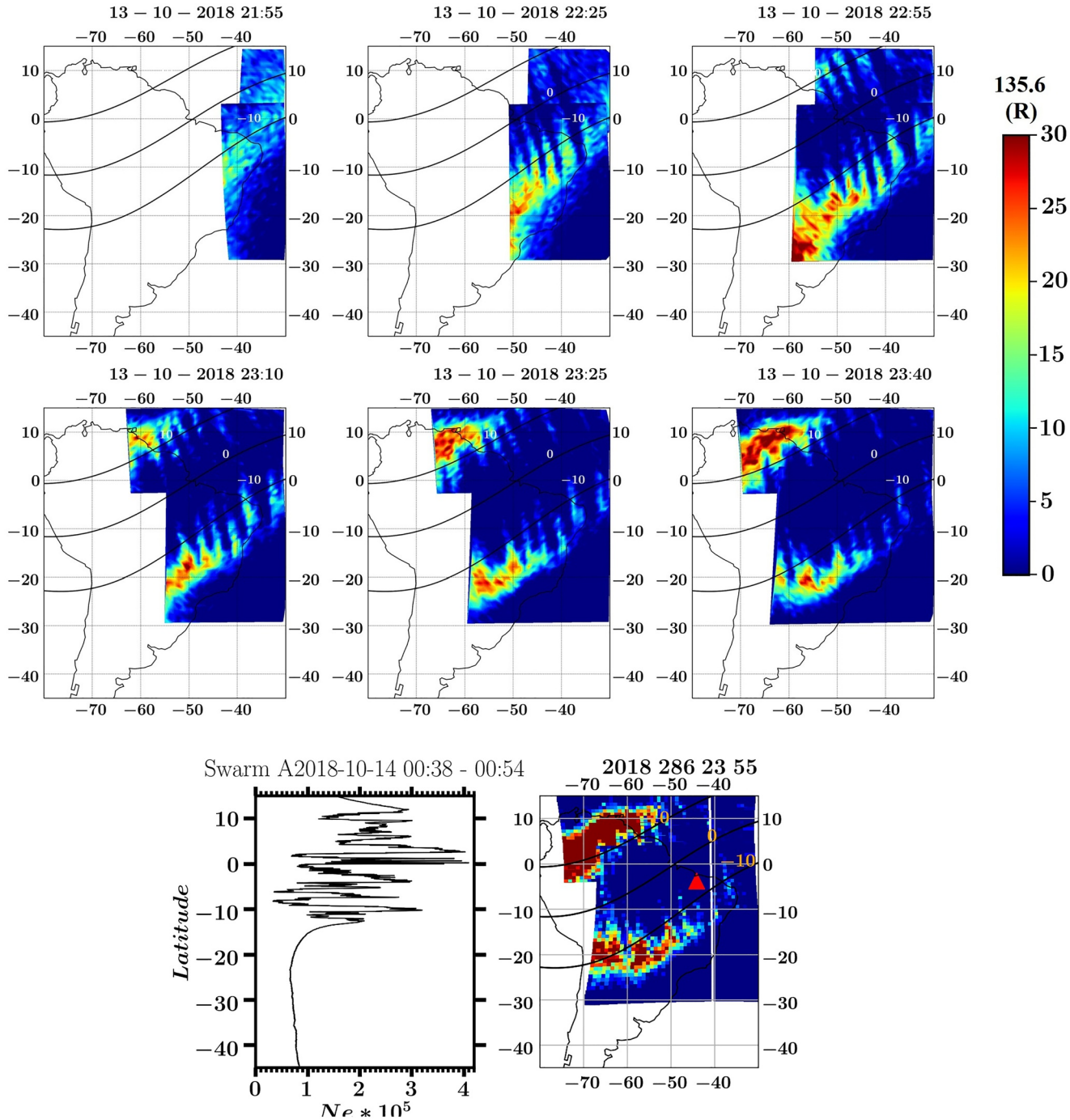

Figure 6. (Top and middle panels) Global-scale Observations of Limb and Disk OI 135.6-nm airglow emission (Rayleighs) from 21:55 to 23:40 UT (18:55 to 20:40 LT) on 13 October 2018 showing the post-sunset equatorial ionization anomaly (EIA) (bright red) and plasma depletions associated with equatorial plasma bubbles (dark blue). (Bottom panels) latitudinal fluctuations of the electron density, Ne, at ~500 km obtained from the SWARM satellite observations during a pass over Brazil between 00:38 and 00:54 UT (21:38 and 21:54 LT) over ~39°W longitude, indicated by the white vertical line. The horizontal and vertical axes represent the geographic longitude and latitude respectively. The three black curves represent ±10° dip latitude and the geomagnetic equator (central curve). Both maps show the post-sunset EIA was located between 20°N and 20°S dip latitude at ~20:55 LT.

Rayleighs (15 at the wall, 5 within the bubble) while for TEC it is around 15 TECU. On a quiet night (6 October), the depletions/EPBs have a magnitude of ~8 TECU against a background of 16 TECU (~8 TECU). The depletions measured by GOLD at ~300 km altitude seem to be deeper than those detected in the TEC. One importance of GNSS is that it offers continuous monitoring of the ionosphere while GOLD is limited to the

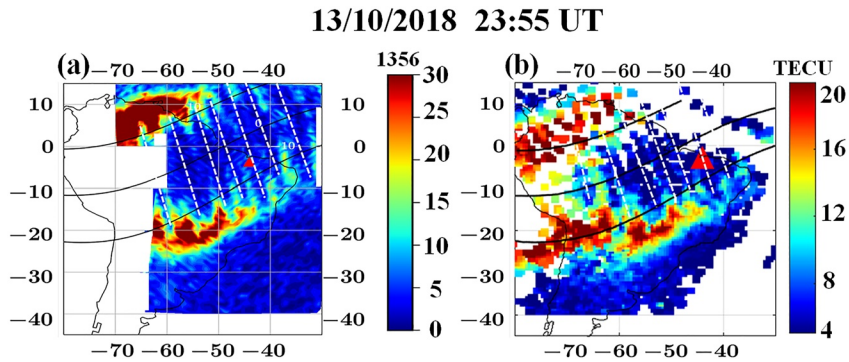

Figure 7. Global-scale Observations of Limb and Disk 135.6 nm radiance map showing a 15-min scan which began at 23:55 UT and Total Electron Content map on the night on 13 October 2018. Plasma depletions are marked by dashed lines.

local pre-midnight sector ~20:10 to 24:25 UT (17:10 LT–21:25 LT) (Eastes et al., 2019). However, during solar minimum EPBs usually occur from the local sunset, ~21:00 UT (18:00 LT) to local midnight (Sobral et al., 2002) hence the observation period of GOLD is within the time interval where the evolution of the EPBs can be shown. GOLD provides insight into the finer morphology of EPBs over the eastern coast and northern part of South America which was previously not well known. EPBs extend beyond ~45°W and are therefore not only a threat to inland navigation and positioning systems but also over the Atlantic Ocean.

3.4. Small-Scale Ionospheric Irregularities

In this section, we discuss the strength of small-scale irregularities according to the GNSS ROTI. Rate of TEC index is used to describe the dynamic changes in electron density and to investigate the presence of small-scale irregularities (~km) associated with EPBs at low latitudes (Pi et al., 1997). Moreover, GNSS receivers are more widely available than scintillation monitors hence ROTI is considered a good tool to study radio scintillation associated with ionospheric irregularities.

Figure 8 shows a sequence of maps showing the temporal variation in post-sunset ROTI obtained from ground-based GNSS receivers in Brazil. Strong, irregularities (ROTI > 0.2) began at 22:25 UT (19:25 LT) over the eastern sector of Brazil while weak and smaller amplitude was detected on a quiet day. The structures extend beyond 15°S dip latitude while on 6 October they were only limited to 10°S dip latitude. The amplitude of the irregularities was located over low latitudes where plasma density gradients are generally larger (Abdu et al., 2009b). At 22:55 UT (19:55 LT)

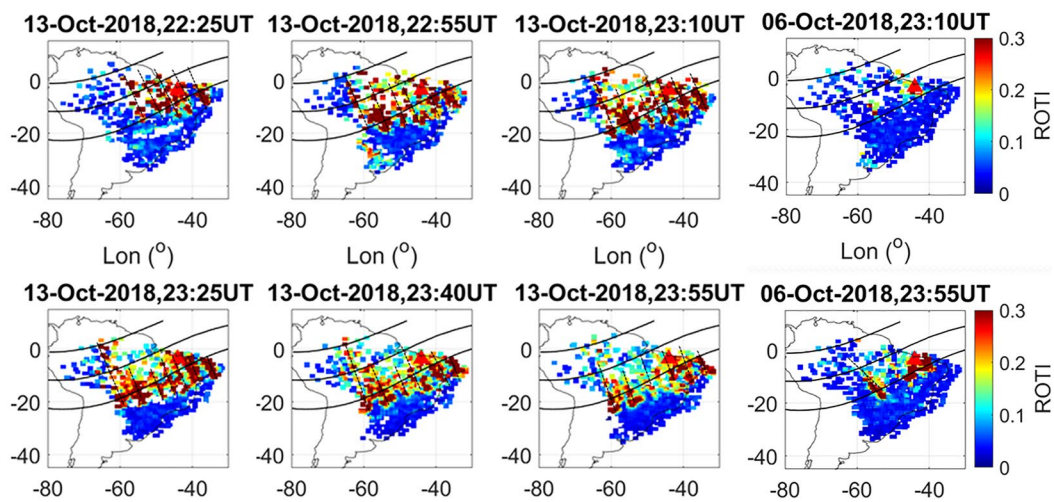

Figure 8. Maps of the Rate of TEC index (ROTI) calculated from Global Navigation Satellite Systems receivers in Brazil on 13 October; (first three panels) and 6 October 2018 (last panel) showing the presence of strong, periodic irregularities (ROTI > 0.2) highlighted by the black dashed lines.

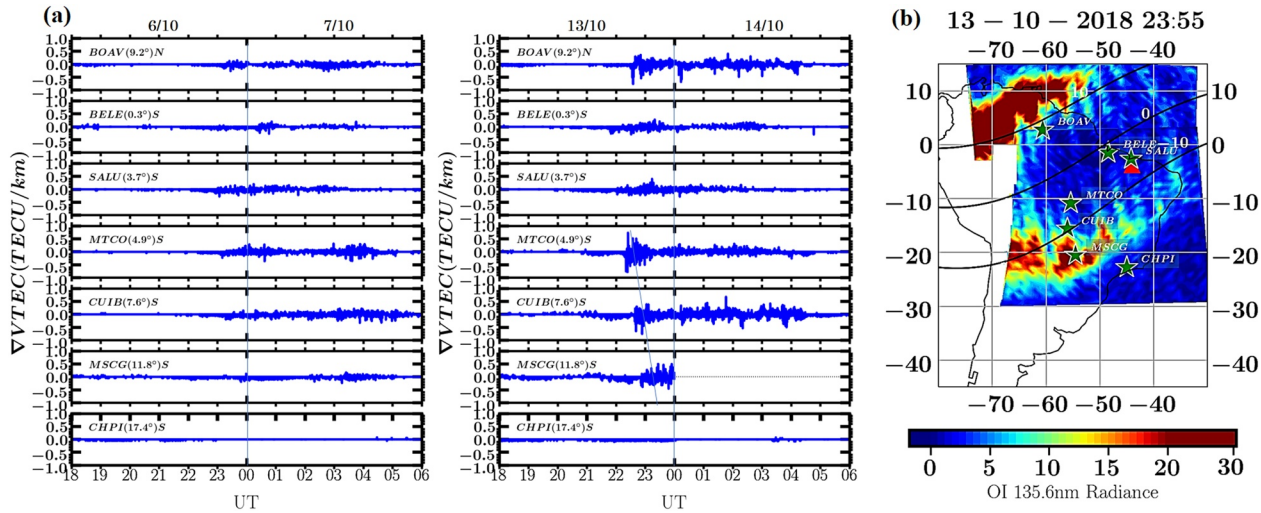

Figure 9. (a) Left and middle panels: Spatial and hourly Total Electron Content gradients (time-step method) calculated at five representative stations with the dip latitude indicated in brackets for the nights of 06–07 (quiet day) and 13–14 October, (b) Global-scale Observations of Limb and Disk FAR UV 135.6 nm emission image at ∼23:55 (20:55 LT) showing plasma depletions and the nighttime equatorial ionization anomaly. The locations of the stations are also shown on the map.

ROTI increased as the irregularities expanded poleward. Thereafter the amplitude decreased at 23:25 UT (20:25 LT) over the equatorial region while some irregularities remained over the EIA. Small-scale irregularities were also detected by the SWARM *Ne*, although the ROTI maps indicate irregularities lasted until ∼05:00 UT (02:00 LT) the next day. Furthermore, the irregularities show similar temporal and spatial distribution to the EPB depletions observed in GOLD and GNSS TEC maps, however, they are smaller in size and have a shorter longitudinal separation. Although regular spacing in large-scale plasma bubbles has previously been detected using other instruments (Eastes et al., 2019; Takahashi et al., 2018), this is the first time that periodic spacing of smaller-scale irregularities is shown in such fine detail consistent with the large-scale bubbles detected by GOLD OI 135.6 nm radiance maps.

3.5. Ionospheric Gradients in TEC

After analyzing the time of occurrence and location of ionospheric irregularities, we analyze the behavior of the spatial gradients in TEC. Figure 9 shows VTEC variation on, the night of 6–7 October (quiet reference) and on 13–14 October 2018, during the first 2 hr of the storm RP. The GOLD FUV OI 135.6 nm emission image at 23:55 UT (20:55 LT) on the right shows depletions/EPBs (dark blue) over the representative stations located north and south of the magnetic equator. Plasma irregularities were detected on both days. However, VTEC was larger on the disturbed day during the post-sunset to post-midnight sector (∼22:00–05:00UT, 19:00–02:00 LT) and peaked earlier in comparison to quiet time. The magnitude of the TEC gradients was also stronger at the crests of EIA (BOAV, MTCO, and MSCG) compared to the equatorial sector (BELE, SALU). The gradients were observed simultaneously with the EPBs although they continued up to the next day. There is no evidence of TEC gradients at around CHPI, indicating that this station was outside the latitudinal extent of the EPBs, as shown in the GOLD OI 135.6 nm image. Sharper edge gradients can be observed at the side walls of the EPBs compared to those observed inside the bubbles (Pimenta et al., 2001; Pradipta & Doherty, 2016).

The EIA is the region where EPBs and gradients most severely impact the performance of GNSS and GBAS (Datta-Barua et al., 2002; Lee et al., 2006; Pradipta & Doherty, 2016). As expected, the strongest TEC gradients coincide with the maxima in the ROTI. Although plasma density is lower during solar minimum, our observations show that the occurrence of a minor geomagnetic storm can affect the conditions for the plasma bubbles occurrence such as enhancement in TEC and a prolonged postsunset EIA. These gradients can affect GNSS, and GBAS systems, causing navigation errors or critical system failure while changes in thermospheric composition enhance orbital drag, potentially leading to the loss of satellites.

3.6. F-Layer Heights, Plasma Frequencies, and Equatorial Electrojet Strength

A large positive ionospheric storm, of amplitude ∼23 TECU, was observed mainly at the crests of the EIA over South America. In addition, there was development of EPBs early into the Spread-F season (October) together

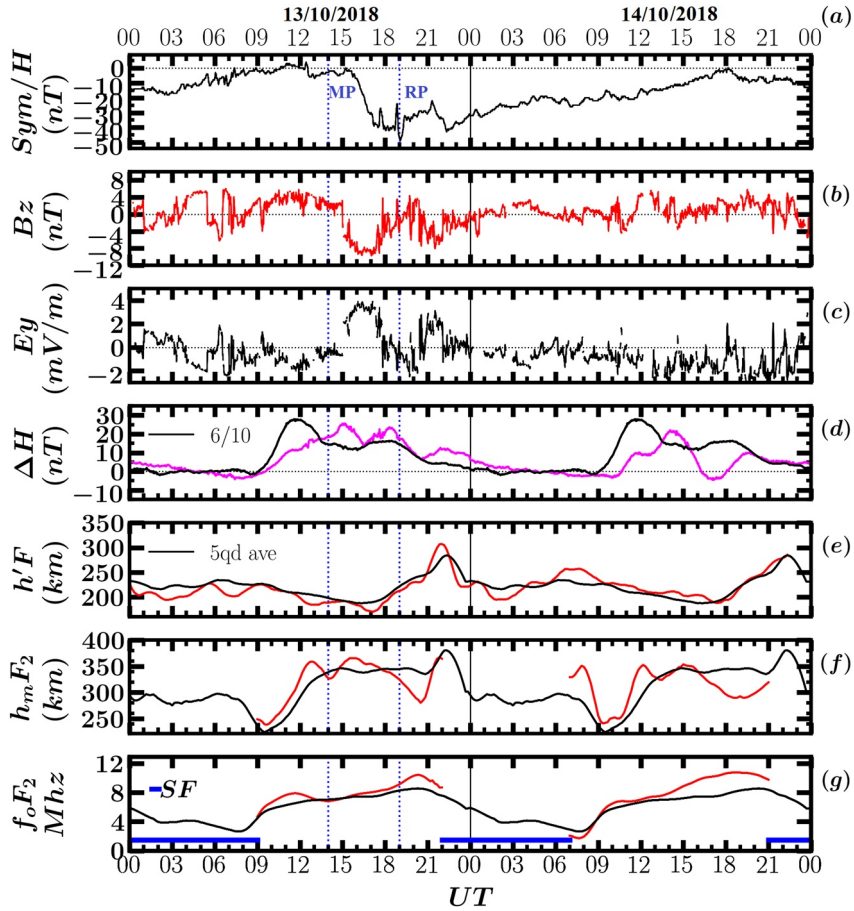

Figure 10. Variations of (a) *Sym-H*, (b) B_z, (c) Ey, (d) ΔH (*SLZ-VSS*) (magenta during the storm days with a quiet reference day on 6 October 2018 in black), (e) the F-layer virtual height, $h'F$, (f) peak height, h_mF_2, and (g) critical frequency, foF_2 for São Luís. The black curves represent the average of the five quietest geomagnetic days in the (5QD) for each parameter. The vertical dashed lines show the beginning of the main and the recovery phases, respectively. The blue horizontal bar in the bottom panel indicates the time interval of Spread-F (SF).

with the strengthening of plasma TEC irregularities and gradients. The ∑O/N2 was partly responsible for the TEC enhancement during the daytime. Apart from thermospheric composition changes, penetration electric fields also play an important role in low-latitude electrodynamics that control the development of the EIA and plasma irregularities (Fejer, 2011). We investigate the behavior of the F layer parameters obtained from a digisonde located in the equatorial sector.

Figure 10 shows, from top to bottom panels the temporal variation of (a) the Sym-H, (b) the vertical component of the IMF B_z, (c) the interplanetary electric field E_y; (d) the EEJ strength, ΔH, in comparison with the quiet day, 6 October 2018 (black curve); (e) the F-layer virtual height, $h'F$, peak height, h_mF_2, and the critical frequency, f_0F_2.

On 13 October from 20:40 to 22:00 UT, there was a sharp increase in $h'F$ from 230 to 310 km soon after a sudden decrease in the h_mF_2 from 350 km (18:00 UT, 15:00 LT) to 285 km (20:30 UT, 17:30 LT). The PRE peak in $h'F$ occurred 1 hour earlier than the 5QD (black line) during which there was a sudden southward turning of B_z from 20:30 to 22:00 UT (17:30 to 19:00 LT). On 14 October the $h'F$ variation was similar to quiet time, with no noticeable increase at the PRE. During the MP, h_mF_2 increased from 350 to 375 km over 1.5 hr and peaked around 15:30 UT (12:30 LT). However, there was a downward movement in the bottom side of the F layer ($h'F$) from 16:00 to 18:00 UT (13:00 to 15:00 LT) when the PS in TEC was strongest as seen in Figure 4b. On 14 October there was an upward movement in the h_mF_2 until 15:00 UT (noon LT) when it was reversed downward. A positive storm seen in f_0F_2 occurred in both the main (MP) and recovery (RP) phases after 14:00 UT (11:00 LT) and 14:00 UT (11:00 LT), respectively, but this effect was less pronounced on 13 October (MP). In both cases, there was a significant

drop in the h_mF_2. During the MP, this movement was more abrupt and late, reaching a minimum of 280 km at 20:30 UT. Before sunset, there was a bump in f_0F_2 simultaneously there was a strong positive storm in TEC over equatorial and low latitudes (see Figure 4b) which peaked at 20:30 UT (17:30 LT). On 14 October, at the end of the RP, the h_mF_2 at around 15:00–21:00 UT the h_mF_2 decreased from 350 to 280 km while f_0F_2 increased. This is a typical indicator suppression of the $E \times B$ drift.

Figure 10d shows enhancement in the ΔH at 13:30 UT (10:30 LT), with peaks at 15:00 UT (noon LT) and 18:30 UT (15:30 LT). This increase lasted up to the end of the MP at 19:30 UT (16:30 LT). The large PS in ΔTEC and strengthening of the EIA around 17:00 UT (14:00 LT) coincide with the two peaks in the ΔH during the MP, both accompanied by the negative excursion of the B_z and the auroral electrojet intensification (Figure 3).

An increase in ΔH indicates an enhancement in the EEJ, which is responsible for the fountain effect and development of the EIA. A sudden southward turning of B_z is a condition for the undershielding PPEF, which enhances the $E \times B$ drift and leads to poleward expansion of the EIA crests in comparison with the quiet time, as was observed in TEC maps, also reported by Astafyeva et al. (2015), Blanc and Richmond (1980), Enge et al. (2013) and J. Y. Liu et al. (1999). de Abreu et al. (2010) and Fagundes et al. (2016) reported large PS in TEC and expansion in the EIA region over South America under eastward PPEF which is typical of geomagnetic disturbances over low latitudes (Abdu, 1997). After the sunset and near the PRE, ∼21:00 UT (18:00 LT) there was another increase in the ΔH which lasted up to 03:00 UT (00:00 LT) on 14 October. The enhanced PRE, in comparison to quiet reference day, is caused by the strengthening of $E \times B$ drift, which is responsible for the observed F layer uplift in $h'F$ after the sunset (Figure 8e). This is a clear effect of the eastward undershielding PPEF during the MP of the storm. On the other hand, at the beginning of the RP, a PS at the magnetic equator concurrent with a decrease in h_mF_2 is caused by the counter-electrojet which suppresses the fountain effect (Sharma et al., 2011). This usually occurs in the RP of geomagnetic storms driven by a DDEF of westward polarity during the day (Blanc & Richmond, 1980).

The estimated vertical $E \times B$ drift velocity from Digisonde measurements shows that during the quiet time, it reached a PRE maximum (v_p) of 20 m/s at 23:00 UT (20:00 LT). In comparison, the average v_p for the month was ∼22 m/s hence the quiet day is a fair representation of quiet time behavior. On 13 October, v_p reached 39 m/s at 21:30 UT (18:30 LT) and the PRE occurred ∼1 hr 30 min earlier than the quiet time. The increase in ΔH implies an enhanced zonal eastward electric field by PPEF which caused a larger v_p at the PRE resulting in the rapid uplift of the F layer. de Abreu et al. (2011) and Aa et al. (2020) found that peak vertical drifts can increase up to ∼30 m/s over São Luís during a minor geomagnetic disturbance period, consistent with our findings. The vertical drift at the PRE is a critical factor in the formation of RT (Aa et al., 2020; de Paula et al., 2019; Kelley, 2009; Pimenta et al., 2008). The maximum drift velocity determines the equatorial apex height of the EPBs after which they diffuse along the field lines. Thus, it controls the latitudinal extension of the EPBs (Abdu et al., 2009a). Consequently, irregularities had a larger latitudinal extension in comparison with the quiet day as shown in the ROTI. In addition, Spread-F in ionograms and depletions in OI 630 nm from an All-sky emission imager were detected from 21:50 to 07:00 UT (18:50 to 04:00 LT) (see Figure S1 in Supporting Information S1).

3.7. Gravity Wave as Seeding Mechanism for Equatorial Plasma Bubbles

Our observations using GOLD FAR UV 135.6 nm images and TEC maps revealed periodically spaced depletions, as reported by Eastes et al. (2019). This has been attributed to the oscillations in the F-region bottomside caused by gravity waves which have been covered extensively in Abdu et al. (2009a), Ajith et al. (2020), Hysell et al. (1990), Kelley and McClure (1981), Takahashi et al. (2009, 2015) and the references therein. Ajith et al. (2020) pointed out the possible seeding of the Rayleigh Taylor instability by gravity waves. We examine the behavior of F-layer true heights provided by an inversion algorithm using the *SAO Explorer software* (Huang & Reinisch, 1996). The true heights were used for estimating the vertical drift (dhF/dt) and detecting oscillations due to GWs at fixed frequencies (5–8 MHz) (isolines). These were also band-pass filtered (20 min–3 hr) (Abdu et al., 2009b). The same filter was applied to the TEC data. The same filter was applied to the TEC data.

Figure 11 (left) shows a sinusoidal oscillation at multiple frequencies with a periodicity of ∼50 min and amplitude of ∼30 km with a downward propagating phase at 18:00 UT (15:00 LT)–03:00 UT (00:00 LT). The same structure can be observed in TEC. This is the signature of propagating gravity wave structures in the F layer near sunset (Abdu et al., 2009a; Jonah et al., 2016). Several studies reported that large-scale periodic wave structures

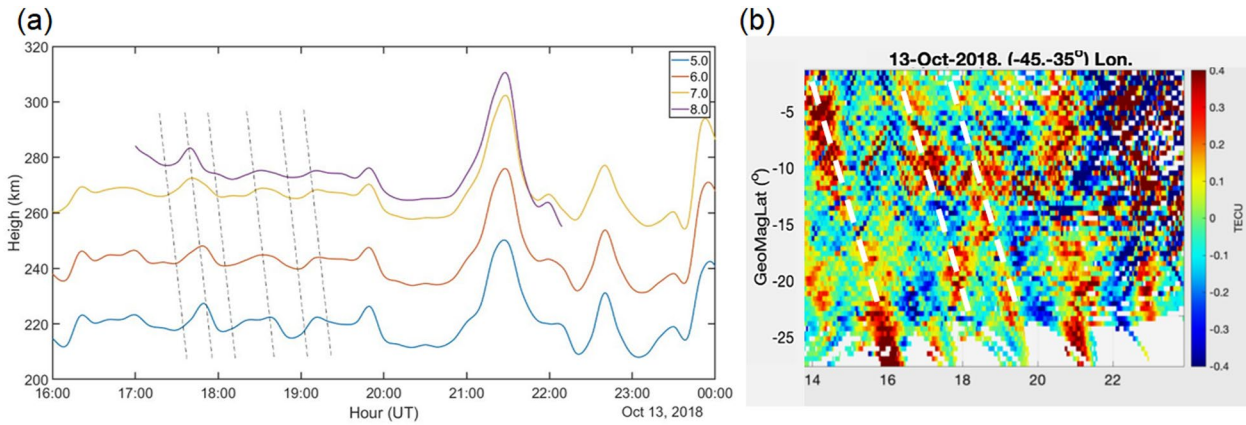

Figure 11. (a) Left: Band-pass filtered (20 min–3 hr) of F layer true heights at four fixed frequencies, 5−8 MHz, over São Luís. Downward phase propagation is shown by the traces. (b) Right: Latitudinal variation (hodogram) of detrended Total Electron Content between 14:00 and 24:00 UT (11:00–21:00 LT), on 13 October, for 45°W–35°W longitude showing wave-like oscillations (Traveling ionospheric Disturbances) just before the sunset.

precede EPBs (Aa et al., 2019; Abdu et al., 2009a; Takahashi et al., 2018). The horizontal wavelength of TIDs (not inferred here) is correlated to the separation between adjacent plasma bubbles (Takahashi et al., 2009, 2018). Aa et al. (2020) estimated an inter-bubble distance of ∼500–800 km over South America in late October 2018 using GOLD OI 135.6 nm and TEC maps under geomagnetically quiet conditions consistent with previous studies (Barros et al., 2018; Takahashi et al., 2018). We inferred a smaller inter-bubble distance of ∼250–700 km which varied with longitude. The shortest separation was over the middle sector of South America (45°W–55°W) which suggests that TIDs that seeded EPBs on that day possibly had shorter horizontal wavelengths.

4. Discussion

The effects of a minor CIR-driven geomagnetic storm during solar minimum 2018 on the Brazilian low latitude ionosphere were investigated using multiples techniques: TEC and its derived parameters; ΔTEC, ROTI, and ∇TEC; GOLD OI 135-6 nm maps; SWARM electron density; H-component from magnetometers, and F-region parameters taken from Digisonde near the equatorial region. Our results show a large positive ionospheric storm (∼23 TECU) during the main and recovery phases on 13–14 October, at 19:00 UT (16:00 LT). The main mechanisms responsible for the remarkable changes in the ionosphere were: (a) the strengthening of the fountain effect indicated by the expansion of the EIA due to PPEF, and (b) thermospheric neutral composition changes seen on ΣO/N2 column which led to a large PS. The intensification of TEC and expansion of the EIA during the disturbed interval over the Brazilian equatorial and low latitudes have been previously reported (de Abreu et al., 2017; Fagundes et al., 2016; Moro et al., 2021; Sharma et al., 2011; J. Liu et al., 2012). In addition, we observed a long-lived, nighttime EIA. Eastes et al. (2019) observed large variability in the post-sunset EIA under very quiet conditions ($1 < K_p < 2$) using GOLD OI 135.6 nm. They reported shifting of the EIA to higher latitudes during an interval of sporadic B_z negative which is an indicator of eastward PPEF. The effects of PPEF are usually short-lived, lasting from a few minutes to hours after the storm's onset (Kelley et al., 2003). However, the PS in TEC lasted began in the MP and lasted up to the next day, well into the RP (23:40 UT, 20:40 LT) indicating a different mechanism.

Changes in the ∑O/N2 density ratio driven by thermospheric winds are mainly responsible for low and middle-latitude ionospheric effects during the RP of the storms. Enhancements in the thermospheric composition over low latitudes during deep solar minimum (F10.7–69 SFU) can contribute significantly to the PS (Cai et al., 2021). Global changes in ∑O/N2 during an intense (SymH ∼207 nT) CME-driven storm in the same year during August 2018 were reported by Astafyeva et al. (2015), Kumar and Kumar (2019), Moro et al. (2021). Since the storm occurred under similar solar flux conditions, we can compare the impact of this intense CME-driven storm with that of the minor CIR-driven storm. Astafyeva et al. (2020) observed a PS of ∼5 TECU at low latitudes and Moro et al. (2021) reported a PS in the f_0F_2 together with the poleward expansion of the EIA crests in the Brazilian sector attributed to a combination of ∑O/N2 enhancement and an eastward PPEF (J. Liu et al., 2012). They also observed that the largest PS in (f_0F_2) occurred during the RP. Cai et al. (2021) reported 2 cases of a

~30% long-lasting increase in TEC related to ∑O/N2 over mid-latitude during weak geomagnetic disturbances (K_p < 2). The ∑O/N2 variations were generated at high latitudes and subsequently transported equatorward. Astafyeva et al. (2020) also reported significant depletions in the O/N2 ratio over low-to-high latitudes which were then displaced equatorward by disturbance thermospheric winds. Thermospheric changes and winds are associated with Joule heating at auroral latitudes (Cai et al., 2020b; Fuller-Rowell et al., 1996). Although these effects originate from high latitudes, they can still reach mid and low latitudes under the influence of equatorward neutral winds by horizontal advection (Astafyeva et al., 2020; Cai et al., 2020b; Danilov et al., 1994; Fuller-Rowell et al., 1996). Therefore, our observations indicate that the positive ionospheric storm, PS, was due to the combination of an increase in the thermosphere composition ∑O/N2 ratio and an eastward PPEF. However, there are several competing processes at equatorial and low latitudes such as PPEFs, disturbance dynamo electric fields, DDEFs, meridional winds (Balan et al., 2013) as well as thermospheric composition changes. As such quantifying the individual contributions of each mechanism remains a challenge (Moro et al., 2021).

Moreover, the effects of geomagnetic storms on changes in the neutral thermosphere are more significant during solar minimum compared to solar maximum as equatorward winds are more effective (Burns et al., 2004). Burns et al. (2004) also found that the spatial extent of enhancements in storm-time O/N2 ratio is much more restricted in winter than in summer likely due to seasonal differences in thermosphere circulation patterns (Fuller-Rowell et al., 1996) which could also explain the larger PS in the CIR storm compared to the winter CME storm. During the minor CIR-driven storm, the strengthening of the EEJ shown by an increase in ΔH, was responsible for the expansion of the EIA, whereas, during the intense storm, the magnetic field hardly deviated from the quiet-time levels (Astafyeva et al., 2020). This could explain the large PS in the MP of the CIR storm in contrast to a weaker enhancement in TEC during the CME. This is evidence that the PPEF was more effective during the minor storm causing an intense daytime ionospheric response and stronger post-sunset irregularities as opposed to the weaker response during the CME storm (Astafyeva et al., 2020). Despite the small magnitude of the geomagnetic storm and the weak background conditions characterized by solar minimum, there was a very large increase in the TEC (~23 TECU) during the daytime and a prolonged EIA at night in comparison with the quiet geomagnetic day.

Although the minor storm occurred during the early Spring equinox, which is the EPBs/Spread F season, such large enhancements are very rare considering the magnitude of the CIR-storm and low solar flux, F10.7–70 SFU (Cai et al., 2020b; Cai et al., 2021). Dugassa et al., 2020 also observed that a CIR-driven storm in the equinox greatly enhanced the EIA and irregularities over the American sector compared to a larger magnitude CME-driven storm during winter which is contrary to what is expected. Our findings are also in agreement with these observations. Finally, wave-like oscillations were simultaneously observed in F-layer true heights TEC over the same region, with periods ~45 min are typical of GWs. Periodic depletions were also seen in GOLD 135.6 nm and TEC maps. To the best of our knowledge, it is the first time that coincident ground- and space-based are used to investigate the characteristics of EPBs in the Brazilian sector. It is also important to note that, besides the storm magnitude, other factors such as the storm onset time (Dugassa et al., 2020), longitude, and solar activity contribute to the background quiet time conditions that control ionospheric response (Burns et al., 2004). The seasonality of geomagnetic activity (Russell & McPherron, 1973) also seems to have a major role in the ionospheric response.

5. Summary and Conclusion

In this work, we presented a multiple-approach investigation of the Brazilian low-latitude ionosphere response to a minor geomagnetic CIR/HSS-driven storm during solar minimum 2018. Our findings are summarized as follows:

1. An unexpected large ionospheric storm (>20 TECU) over the Brazilian low latitude was caused by a minor (G1) CIR/HSS-driven geomagnetic storm.
2. The largest PS occurred due to the combination of under-shielding eastward PPEF and an enhancement in the thermosphere composition ratio [O]/[N2].
3. Storm-time PPEF triggered periodic, large-scale plasma depletions observed in the GOLD OI 135.6 nm emissions and GNSS-TEC maps while intensification of small-scale irregularities was detected in the ROTI.
4. Periodically spaced large-scale depletions and irregularities associated with TIDs were detected in oscillations of the F layer, and detrended TEC.

5. Stronger gradients in TEC at the crests of EIA confirm the impact of a CIR minor storm at the low latitude region.

In conclusion, the strengthening of ionospheric irregularities and TEC gradients during the storm is of great interest to GNSS/GBAS operations while increases in the orbital drag due to thermosphere composition changes impact satellites in orbit. It is important to note that, GNSS-TEC receivers are scarce in the northern part of Brazil. The GOLD mission can be utilized to study the Brazilian low-latitude region. Rate of TEC index on the other hand is also a powerful tool to identify the occurrence of EPBs and the detection of radio wave scintillation in areas where high-cost scintillation monitors are otherwise scarce. We highlight the importance of studying minor and moderate storms driven by CIR/HSSs during low solar activity, which is of great interest to space weather, particularly with the rapidly increasing number of satellites in low earth orbit.

Data Availability Statement

The solar wind and IMF data were provided by the NASA CDAWeb (https://cdaweb.gsfc.nasa.gov/pub). We used the SYM-H and AE with the 1-min resolution provided by the World Data Center for Geomagnetism, WDC, Kyoto University (http://wdc.kugi.kyoto-u.ac.jp/index.html). Coronal hole (CH) images were provided by (solar-monitor.org), hosted by Dublin Institute for Space Studies. The High-Speed Streams detection and properties as well as their source CH were obtained from the Solen website (https://www.solen.info/solar/). The Receiver Independent Exchange Format, Rinex, data used for GNSS-TEC calculation were obtained from (https://www.ibge.gov.br/ and http://cedar.openmadrigal.org/). The Horizontal component of the geomagnetic field and Al-lsky images were downloaded from the EMBRACE network (http://www2.inpe.br/climaespacial/SpaceWeatherData-Share) and INTERMAGNET (https://www.intermagnet.org/data-donnee/download-eng.php). The OI 135.6 nm airglow emission and thermospheric column ratio [O]/[N2] was obtained from NASA GOLD Far Ultra-violet imager available at https://gold.cs.ucf.edu/search. Digisonde data was obtained from the UML Digital Ionogram (http://ulcar.uml.edu/DIDBase/; http://spase.info/SMWG/Observatory/GIRO). The SWARM electron density data were obtained from the ESA website (https://swarm-diss.eo.esa.int/).

Acknowledgments
This study was supported by Coordenação de Aperfeiçoamento de Pessoal de Nível Superior (MCTI/CAPES)—Grant 88882.330722/2019-01. The authors also thank the INCT GNSS-NavAer supported by CNPq (465648/2014-2), FAPESP (2017/50115-0), and CAPES (88887.137186/2017-00). The authors wish to express their sincere thanks to the IBGE (http://www.ibge.gov.br/home/geociencias/geodesia/rbmc/rbmc_est.php) and Madrigal for providing GPS-TEC data. We would like to thank the EMBRACE/INPE for providing the All-sky imager and Ionosonde data. We gratefully acknowledge the GFSC NASA OMNIWEB and the Kyoto World Data Center for Geomagnetism for the K_p index. We gratefully acknowledge the NASA GOLD Mission.

References

Aa, E., Zhang, S., Erickson, P. J., Coster, A. J., Goncharenko, L. P., Varney, R. H., & Eastes, R. (2021). Salient midlatitude ionosphere-thermosphere disturbances associated with SAPS during a minor but geo-effective storm at deep solar minimum. *Journal of Geophysical Research: Space Physics*, *126*(7), e2021JA029509. https://doi.org/10.1029/2021JA029509

Aa, E., Zou, S., Eastes, R., Karan, D. K., Zhang, S. R., Erickson, P. J., & Coster, A. J. (2020). Coordinated ground-based and space-based observations of equatorial plasma bubbles. *Journal of Geophysical Research: Space Physics*, *125*(1), 1–13. https://doi.org/10.1029/2019JA027569

Aa, E., Zou, S., Ridley, A., Zhang, S., Coster, A. J., Erickson, P. J., et al. (2019). Merging of storm time midlatitude traveling ionospheric disturbances and equatorial plasma bubbles. *Space Weather*, *17*(2), 285–298. https://doi.org/10.1029/2018SW002101

Abdu, M. A. (1997). Major phenomena of the equatorial ionosphere-thermosphere system under disturbed conditions. *Journal of Atmospheric and Solar-Terrestrial Physics*, *59*(13), 1505–1519. https://doi.org/10.1016/s1364-6826(96)00152-6

Abdu, M. A. (2001). Outstanding problems in the equatorial ionosphere–thermosphere electrodynamics relevant to spread F. *Journal of Atmospheric and Solar-Terrestrial Physics*, *63*(9), 869–884. https://doi.org/10.1016/s1364-6826(00)00201-7

Abdu, M. A., Alam Kherani, E., Batista, I. S., de Paula, E. R., Fritts, D. C., & Sobral, J. H. A. A. (2009a). Gravity wave initiation of equatorial spread F/plasma bubble irregularities based on observational data from the SpreadFEx campaign. *Annales Geophysicae*, *27*(7), 2607–2622. https://doi.org/10.5194/angeo-27-2607-2009

Abdu, M. A., Batista, I. S., Reinisch, B. W., de Souza, J. R., Sobral, J. H. A. A., Pedersen, T. R., et al. (2009b). Conjugate Point Equatorial Experiment (COPEX) campaign in Brazil: Electrodynamics highlights on spread F development conditions and day-to-day variability. *Journal of Geophysical Research*, *114*(A4). https://doi.org/10.1029/2008JA013749

Abdu, M. A., Bittencourt, J. A., & Batista, I. S. (1981). Magnetic declination control of the equatorial F region dynamo electric field development and spread F. *Journal of Geophysical Research*, *86*(A13), 11443. https://doi.org/10.1029/ja086ia13p11443

Ajith, K. K., Li, G., Tulasi Ram, S., Yamamoto, M., Hozumi, K., Abadi, P., & Xie, H. (2020). On the seeding of periodic equatorial plasma bubbles by gravity waves associated with tropical cyclone: A case study. *Journal of Geophysical Research: Space Physics*, *125*(10), 1–15. https://doi.org/10.1029/2020JA028003

Anderson, D., Anghel, A., Yumoto, K., Ishitsuka, M., & Kudeki, E. (2002). Estimating daytime vertical ExB drift velocities in the equatorial F-region using ground-based magnetometer observations. *Geophysical Research Letters*, *29*(12), 37-1–37-4. https://doi.org/10.1029/2001GL014562

Astafyeva, E., Bagiya, M. S., Förster, M., & Nishitani, N. (2020). Unprecedented hemispheric asymmetries during a surprise ionospheric storm: A game of drivers. *Journal of Geophysical Research: Space Physics*, *125*(3), 1–15. https://doi.org/10.1029/2019JA027261

Astafyeva, E., Zakharenkova, I., & Förster, M. (2015). Ionospheric response to the 2015 St. Patrick's Day storm: A global multi-instrumental overview. *Journal of Geophysical Research: Space Physics*, *120*(10), 9023–9037. https://doi.org/10.1002/2015JA021629

Balan, N., Otsuka, Y., Nishioka, M., Liu, J. Y., & Bailey, G. J. (2013). Physical mechanisms of the ionospheric storms at equatorial and higher latitudes during the recovery phase of geomagnetic storms. *Journal of Geophysical Research: Space Physics*, *118*(5), 2660–2669. https://doi.org/10.1002/jgra.50275

Barros, D., Takahashi, H., Wrasse, C. M., & Figueiredo, C. A. O. B. (2018). Characteristics of equatorial plasma bubbles observed by TEC map based on ground-based GNSS receivers over South America. *Annales Geophysicae*, *36*(1), 91–100. https://doi.org/10.5194/angeo-36-91-2018

Bhattacharyya, A., Yeh, K. C., & Franke, S. J. (1992). Deducing turbulence parameters from transionospheric scintillation measurements. *Space Science Reviews*, *61*(3–4), 709–715. https://doi.org/10.1007/BF00222311

Blanc, M., & Richmond, A. D. (1980). The ionospheric disturbance dynamo. *Journal of Geophysical Research*, *85*(A4), 1669–1686. https://doi.org/10.1029/ja085ia04p01669

Burns, A. G., Killeen, T. L., Carignan, G. R., & Roble, R. G. (1995). Large enhancements in the O/N2 ratio in the evening sector of the winter hemisphere during geomagnetic storms. *Journal of Geophysical Research*, *100*(A8), 14661. https://doi.org/10.1029/94JA03235

Burns, A. G., Killeen, T. L., Wang, W., & Roble, R. G. (2004). The solar-cycle-dependent response of the thermosphere to geomagnetic storms. *Journal of Atmospheric and Solar-Terrestrial Physics*, *66*(1), 1–14. https://doi.org/10.1016/j.jastp.2003.09.015

Cai, X., Burns, A. G., Wang, W., Coster, A., Qian, L., Liu, J., et al. (2020a). Comparison of GOLD nighttime measurements with total electron content: Preliminary results. *Journal of Geophysical Research: Space Physics*, *125*(9), 1–18. https://doi.org/10.1029/2019JA027767

Cai, X., Burns, A. G., Wang, W., Qian, L., Pedatella, N., Coster, A., et al. (2021). Variations in thermosphere composition and ionosphere total electron content under "geomagnetically quiet" conditions at solar-minimum. *Geophysical Research Letters*, *48*(11), e2021GL093300. https://doi.org/10.1029/2021GL093300

Cai, X., Burns, A. G., Wang, W., Qian, L., Solomon, S. C., Eastes, R. W., et al. (2020b). The two-dimensional evolution of thermospheric ∑O/N2 response to weak geomagnetic activity during solar-minimum observed by GOLD. *Geophysical Research Letters*, *47*(18), e2020GL088838. https://doi.org/10.1029/2020GL088838

Candido, C. M. N., Batista, I. S., Klausner, V., de Siqueira Negreti, P. M., Becker-Guedes, F., de Paula, E. R., et al. (2018). Response of the total electron content at Brazilian low latitudes to corotating interaction region and high-speed streams during solar minimum 2008. *Earth Planets and Space*, *70*(1), 104. https://doi.org/10.1186/s40623-018-0875-8

Chou, M. Y., Pedatella, N. M., Wu, Q., Huba, J. D., Lin, C. C. H., Schreiner, W. S., et al. (2020). Observation and simulation of the development of equatorial plasma bubbles: Post-sunset rise or upwelling growth? *Journal of Geophysical Research: Space Physics*, *125*(12), 1–30. https://doi.org/10.1029/2020JA028544

Danilov, A. D., Morozova, L. D., Fuller-Rowell, T. J., Codrescu, M. V., Moffett, R. J., & Quegan, S. (1994). Response of the thermosphere and ionosphere to geomagnetic storms. *Journal of Geophysical Research*, *99*(A3), 3893–3914. https://doi.org/10.1029/93ja02015

Datta-Barua, S., Walter, T., Pullen, S., Luo, M., Blanch, J., & Enge, P. (2002). Using WAAS ionospheric data to estimate LAAS short baseline gradients. In *Proceedings of the 2002 national technical meeting of the Institute of Navigation* (pp. 523–530).

de Abreu, A. J., Martin, I. M., Fagundes, P. R., Venkatesh, K., Batista, I. S., de Jesus, R., et al. (2017). Ionospheric F-region observations over American sector during an intense space weather event using multi-instruments. *Journal of Atmospheric and Solar-Terrestrial Physics*, *156*(February), 1–14. https://doi.org/10.1016/j.jastp.2017.02.009

de Abreu, A. J., Sahai, Y., Fagundes, P. R., Becker-Guedes, F., de Jesus, R., Guarnieri, F. L., & Pillat, V. G. (2010). Response of the ionospheric F-region in the Brazilian sector during the super geomagnetic storm in April 2000 observed by GPS. *Advances in Space Research*, *45*(11), 1322–1329. https://doi.org/10.1016/j.asr.2010.02.003

De Abreu, A. J., Sahai, Y., Fagundes, P. R., De Jesus, R., Bittencourt, J. A., & Pillat, V. G. (2011). An investigation of ionospheric F region response in the Brazilian sector to the super geomagnetic storm of May 2005. *Advances in Space Research*, *48*(7), 1211–1220. https://doi.org/10.1016/j.asr.2011.05.036

de Paula, E. R., de Oliveira, C. B. A. A., Caton, R. G., Negreti, P. M., Batista, I. S., Martinon, A. R. F. F., et al. (2019). Ionospheric irregularity behavior during the September 6–10, 2017 magnetic storm over Brazilian equatorial-low latitudes. *Earth Planets and Space*, *71*(1), 42. https://doi.org/10.1186/s40623-019-1020-z

Derghazarian, S., Hysell, D. L., & Varney, R. H. (2021). Topside measurements at Jicamarca during the 2019–2020 deep solar minimum. *Journal of Geophysical Research: Space Physics*, *126*(12), 1–26. https://doi.org/10.1029/2021JA029695

Dugassa, T., Habarulema, J. B., & Nigussie, M. (2020). Equatorial and low-latitude ionospheric TEC response to CIR-driven geomagnetic storms at different longitude sectors. *Advances in Space Research*, *66*(8), 1947–1966. https://doi.org/10.1016/j.asr.2020.07.003

Eastes, R. W., McClintock, W. E. E., Burns, A. G. G., Anderson, D. N. N., Andersson, L., Codrescu, M., et al. (2017). The global-scale observations of the limb and disk (GOLD) mission. *Space Science Reviews*, *212*(1–2), 383–408. https://doi.org/10.1007/s11214-017-0392-2

Eastes, R. W., Solomon, S. C., Daniell, R. E., Anderson, D. N., Burns, A. G., England, S. L., et al. (2019). Global-scale observations of the equatorial ionization anomaly. *Geophysical Research Letters*, *46*(16), 9318–9326. https://doi.org/10.1029/2019GL084199

Enge, P. K., Kintner, P. M., Kil, H., Beach, T. L., De Paula, E. R., Kelley, M. C., et al. (2013). Ionospheric irregularity behavior during the September 6–10, 2017 magnetic storm over Brazilian equatorial-low latitudes. *Journal of Geophysical Research: Space Physics*, *99*(1), 42. https://doi.org/10.5194/angeo-31-263-2013

Fagundes, P. R., Cardoso, F. A., Fejer, B. G., Venkatesh, K., Ribeiro, B. A. G., & Pillat, V. G. (2016). Positive and negative GPS-TEC ionospheric storm effects during the extreme space weather event of March 2015 over the Brazilian sector. *Journal of Geophysical Research: Space Physics*, *121*(6), 5613–5625. https://doi.org/10.1002/2015JA022214

Fejer, B. G. (2011). Low latitude ionospheric electrodynamics. *Space Science Reviews*, *158*(1), 145–166. https://doi.org/10.1007/s11214-010-9690-7

Figueiredo, C. A. O. B., Takahashi, H., Wrasse, C. M., Otsuka, Y., Shiokawa, K., & Barros, D. (2018). Medium-scale traveling ionospheric disturbances observed by detrended total electron content maps over Brazil. *Journal of Geophysical Research: Space Physics*, *123*(3), 2215–2227. https://doi.org/10.1002/2017JA025021

Fuller-Rowell, T. J., Codrescu, M. V., Rishbeth, H., Moffett, R. J., & Quegan, S. (1996). On the seasonal response of the thermosphere and ionosphere to geomagnetic storms. *Journal of Geophysical Research*, *101*(A2), 2343–2353. https://doi.org/10.1029/95ja01614

Gan, Q., Eastes, R. W., Burns, A. G., Wang, W., Qian, L., Solomon, S. C., et al. (2020). First synoptic observations of geomagnetic storm effects on the global-scale OI 135.6-nm dayglow in the thermosphere by the GOLD mission. *Geophysical Research Letters*, *47*(3), e2019GL085400. https://doi.org/10.1029/2019GL085400

Gibson, S. E., de Toma, G., Emery, B., Riley, P., Zhao, L., Elsworth, Y., et al. (2011). The whole heliosphere interval in the context of a long and structured solar minimum: An overview from Sun to Earth. *Solar Physics*, *274*(1–2), 5–27. https://doi.org/10.1007/s11207-011-9921-4

Hady, A. A. (2013). Deep solar minimum and global climate changes. *Journal of Advanced Research*, *4*(3), 209–214. https://doi.org/10.1016/j.jare.2012.11.001

Hines, C. O. (1960). Internal atmospheric gravity waves at ionospheric heights. *Canadian Journal of Physics*, *38*(11), 1441–1481. https://doi.org/10.1139/p60-150

Huang, X., & Reinisch, B. W. (1996). Vertical electron density profiles from the digisonde network. *Advances in Space Research*, *18*(6), 121–129. https://doi.org/10.1016/0273-1177(95)00912-4

Hysell, D. L., Kelley, M. C., Swartz, W. E., & Woodman, R. F. (1990). Seeding and layering of equatorial spread F by gravity waves. *Journal of Geophysical Research*, *95*(A10), 17253. https://doi.org/10.1029/JA095iA10p17253

Jonah, O. F., Kherani, E. A., & De Paula, E. R. (2016). Observation of TEC perturbation associated with medium-scale traveling ionospheric disturbance and possible seeding mechanism of atmospheric gravity wave at a Brazilian sector. *Journal of Geophysical Research: Space Physics*, *121*(3), 2531–2546. https://doi.org/10.1002/2015JA022273

Kelley, M. C. (2009). The Earth's ionosphere. In *Computer engineering* (2nd ed.).

Kelley, M. C., Makela, J. J., Chau, J. L., & Nicolls, M. J. (2003). Penetration of the solar wind electric field into the magnetosphere/ionosphere system. *Geophysical Research Letters*, *30*(4), 23–25. https://doi.org/10.1029/2002GL016321

Kelley, M. C., & McClure, J. (1981). Equatorial spread-F: A review of recent experimental results. *Journal of Atmospheric and Terrestrial Physics*, *43*(5–6), 427–435. https://doi.org/10.1016/0021-9169(81)90106-9

Klenzing, J., Burrell, A. G., Heelis, R. A., Huba, J. D., Pfaff, R., & Simões, F. (2013). Exploring the role of ionospheric drivers during the extreme solar minimum of 2008. *Annales Geophysicae*, *31*(12), 2147–2156. https://doi.org/10.5194/angeo-31-2147-2013

Kumar, S., & Kumar, V. V. (2019). Ionospheric response to the St. Patrick's day space weather events in March 2012, 2013, and 2015 at southern low and middle latitudes. *Journal of Geophysical Research: Space Physics*, *124*(1), 584–602. https://doi.org/10.1029/2018JA025674

Lee, J., Pullen, S., Datta-Barua, S., & Enge, P. (2006). Assessment of nominal ionosphere spatial decorrelation for LAAS. In *Record—IEEE PLANS, position location and navigation symposium* (pp. 506–514). https://doi.org/10.1109/PLANS.2006.1650638

Liu, H. L. (2016). Variability and predictability of the space environment as related to lower atmosphere forcing. *Space Weather*, *14*(9), 634–658. https://doi.org/10.1002/2016SW001450

Liu, J., Liu, L., Zhao, B., Wei, Y., Hu, L., & Xiong, B. (2012). High-speed stream impacts on the equatorial ionization anomaly region during the deep solar minimum year 2008. *Journal of Geophysical Research*, *117*(10), 1–12. https://doi.org/10.1029/2012JA018015

Liu, J. Y., Tsai, H. F., Wu, C. C., Tseng, C. L., Tsai, L. C., Tsai, W. H., et al. (1999). The effect of geomagnetic storm on ionospheric total electron content at the equatorial anomaly region. *Advances in Space Research*, *24*(11), 1491–1494. https://doi.org/10.1016/S0273-1177(99)00712-7

Matamba, T. M., & Habarulema, J. B. (2018). Ionospheric responses to CME- and CIR-driven geomagnetic storms along 30°E–40°E over the african sector from 2001 to 2015. *Space Weather*, *16*(5), 538–556. https://doi.org/10.1029/2017SW001754

Misra, P., & Enge, P. (2011). *Global positioning system: Signals, measurements, and performance*. Ganga-Jamuna Press. Retrieved from https://books.google.com.br/books?id=5WJOywAACAAJ

Moro, J., Xu, J., Denardini, C. M., Resende, L. C. A., Neto, P. F. B., Da Silva, L. A., et al. (2021). First look at a geomagnetic storm with Santa Maria Digisonde data: F region responses and comparisons over the American sector. *Journal of Geophysical Research: Space Physics*, *126*(1), 1–18. https://doi.org/10.1029/2020JA028663

Pereira, V. A. S., & Camargo, P. O. (2014). Padrões para classificação dos índices de irregularidades da ionosfera: IROT e ROTI. In *Anais do V Simpósio Brasileiro de Ciências Geodésicas e Tecnologias da Geoinformação da Universidade Federal de Pernambuco* (pp. 547–555).

Pesnell, W. D. (2020). Lessons learned from predictions of solar cycle 24. *Journal of Space Weather and Space Climate*, *10*, 60. https://doi.org/10.1051/swsc/2020060

Pi, X., Mannucci, A. J., Lindqwister, U. J., & Ho, C. M. (1997). Monitoring of global ionospheric irregularities using the worldwide GPS network. *Geophysical Research Letters*, *24*(18), 2283–2286. https://doi.org/10.1029/97GL02273

Pimenta, A. A., Fagundes, P. R., Bittencourt, J. A., Sahai, Y., Gobbi, D., Medeiros, A. F., et al. (2001). Ionospheric plasma bubble zonal drift: A methodology using OI 630 nm all-sky imaging systems. *Advances in Space Research*, *27*(6–7), 1219–1224. https://doi.org/10.1016/S0273-1177(01)00201-0

Pimenta, A. A., Kelley, M. C., Sahai, Y., Bittencourt, J. A., & Fagundes, P. R. (2008). Thermospheric dark band structures observed in all-sky OI 630 nm emission images over the Brazilian low-latitude sector. *Journal of Geophysical Research*, *113*(1), 1–9. https://doi.org/10.1029/2007JA012444

Pradipta, R., & Doherty, P. H. (2016). Assessing the occurrence pattern of large ionospheric TEC gradients over the Brazilian airspace. *Navigation*, *63*(3), 335–343. https://doi.org/10.1002/navi.141

Prolss, G. W. (1995). Ionospheric F-region storms. In H. Volland (Ed.), *Handbook of atmospheric electrodynamics*. CRC Press.

Rishbeth, H. (1998). How the thermospheric circulation affects the ionospheric F2-layer. *Journal of Atmospheric and Solar-Terrestrial Physics*, *60*(14), 1385–1402. https://doi.org/10.1016/S1364-6826(98)00062-5

Russell, C. T., & McPherron, R. L. (1973). Semiannual variation of geomagnetic activity. *Journal of Geophysical Research*, *78*(1), 92–108. https://doi.org/10.1029/ja078i001p00092

Seemala, G. K., & Valladares, C. E. (2011). Statistics of total electron content depletions observed over the South American continent for the year 2008. *Radio Science*, *46*(5), 1–14. https://doi.org/10.1029/2011RS004722

Sharma, S., Galav, P., Dashora, N., Alex, S., Dabas, R. S., & Pandey, R. (2011). Response of low-latitude ionospheric total electron content to the geomagnetic storm of 24 August 2005. *Journal of Geophysical Research*, *116*(A5), 1–12. https://doi.org/10.1029/2010ja016368

Sobral, J. H. A. A., Abdu, M. A., Takahashi, H., Taylor, M. J., De Paula, E. R., Zamlutti, C. J., et al. (2002). Ionospheric plasma bubble climatology over Brazil based on 22 years (1977–1998) of 630 nm airglow observations. *Journal of Atmospheric and Solar-Terrestrial Physics*, *64*(12–14), 1517–1524. https://doi.org/10.1016/S1364-6826(02)00089-5

Takahashi, H., Taylor, M. J., Pautet, P.-D. D., Medeiros, A. F., Gobbi, D., Wrasse, C. M., et al. (2009). Simultaneous observation of ionospheric plasma bubbles and mesospheric gravity waves during the SpreadFEx campaign. *Annales Geophysicae*, *27*(4), 1477–1487. https://doi.org/10.5194/angeo-27-1477-2009

Takahashi, H., Wrasse, C. M., Denardini, C. M., Pádua, M. B., de Paula, E. R., Costa, S. M. A., et al. (2016). Ionospheric TEC weather map over South America. *Space Weather*, *14*(11), 937–949. https://doi.org/10.1002/2016SW001474

Takahashi, H., Wrasse, C. M., Figueiredo, C. A. O. B., Barros, D., Abdu, M. A., Otsuka, Y., & Shiokawa, K. (2018). Equatorial plasma bubble seeding by MSTIDs in the ionosphere. *Progress in Earth and Planetary Science*, *5*(1), 32. https://doi.org/10.1186/s40645-018-0189-2

Takahashi, H., Wrasse, C. M., Otsuka, Y., Ivo, A., Gomes, V., Paulino, I., et al. (2015). Plasma bubble monitoring by TEC map and 630 nm airglow image. *Journal of Atmospheric and Solar-Terrestrial Physics*, *130–131*, 151–158. https://doi.org/10.1016/j.jastp.2015.06.003

Titheridge, J. E. (1974). Changes in atmospheric composition inferred from ionospheric production rates. *Journal of Atmospheric and Terrestrial Physics*, *36*(7), 1249–1257. https://doi.org/10.1016/0021-9169(74)90111-1

Tsurutani, B. T., Gonzalez, W. D., Gonzalez, A. L. C., Guarnieri, F. L., Gopalswamy, N., Grande, M., et al. (2006). Corotating solar wind streams and recurrent geomagnetic activity: A review. *Journal of Geophysical Research*, *111*(7), A07S01. https://doi.org/10.1029/2005JA011273

Tsurutani, B. T., Gonzalez, W. D., Gonzalez, A. L. C., Tang, F., Arballo, J. K., & Okada, M. (1995). Interplanetary origin of geomagnetic activity in the declining phase of the solar cycle. *Journal of Geophysical Research*, *100*(A11), 21717–21733. https://doi.org/10.1029/95ja01476

Vadas, S. L. (2007). Horizontal and vertical propagation and dissipation of gravity waves in the thermosphere from lower atmospheric and thermospheric sources. *Journal of Geophysical Research*, *112*(6), 1–23. https://doi.org/10.1029/2006JA011845

Verkhoglyadova, O. P., Tsurutani, B. T., Mannucci, A. J., Mlynczak, M. G., Hunt, L. A., Komjathy, A., & Runge, T. (2011). Ionospheric VTEC and thermospheric infrared emission dynamics during corotating interaction region and high-speed stream intervals at solar minimum: 25 March to 26 April 2008. *Journal of Geophysical Research*, *116*(9), A09325. https://doi.org/10.1029/2011JA016604

Watari, S. (2017). Geomagnetic storms of cycle 24 and their solar sources. *Earth Planets and Space*, *69*(1), 70. https://doi.org/10.1186/s40623-017-0653-z

Erratum

The originally published version of this article contained some errors in the Author Contributions. The following contributions have been corrected: Data curation: F. S. Chingarandi, C. M. N. Candido, F. Becker-Guedes, O. F. Jonah, S. P. Moraes-Santos; Formal analysis: F. S. Chingarandi, C. M. N. Candido, F. Becker-Guedes, O. F. Jonah; Investigation: F. S. Chingarandi, C. M. N. Candido, O. F. Jonah; Methodology: F. S. Chingarandi, C. M. N. Candido, F. Becker-Guedes, O. F. Jonah, V. Klausner; Software: F. S. Chingarandi, O. F. Jonah, V. Klausner; Supervision: C. M. N. Candido, F. Becker-Guedes, O. F. Jonah; Validation: F. S. Chingarandi, C. M. N. Candido, F. Becker-Guedes, O. F. Jonah, V. Klausner; Visualization: F. S. Chingarandi, F. Becker-Guedes, O. F. Jonah; Writing – original draft: F. S. Chingarandi, C. M. N. Candido, F. Becker-Guedes, O. F. Jonah, S. P. Moraes-Santos, O. O. Taiwo. The category Conceptualization was correctly credited to F. S. Chingarandi, C. M. N. Candido, F. Becker-Guedes, O. F. Jonah, S. P. Moraes-Santos, V. Klausner, and O. O. Taiwo. Resources was correctly credited to F. S. Chingarandi, and Writing – review & editing was correctly credited to F. S. Chingarandi, C. M. N. Candido, F. Becker-Guedes, O. F. Jonah, S. P. Moraes-Santos, V. Klausner, and O. O. Taiwo in the originally published version and did not require correction. This may be considered the authoritative version of record.